

# NUCLEOSYNTHESIS IN THE INNERMOST EJECTA OF NEUTRINO-DRIVEN SUPERNOVA EXPLOSIONS IN TWO DIMENSIONS

SHINYA WANAJO,<sup>1,2</sup> BERNHARD MÜLLER,<sup>3,4</sup> HANS-THOMAS JANKA,<sup>5</sup> AND ALEXANDER HEGER<sup>4,6,7</sup>

<sup>1</sup>*Department of Engineering and Applied Sciences, Sophia University, Chiyoda-ku, Tokyo 102-8554, Japan; shinya.wanajo@sophia.ac.jp*

<sup>2</sup>*iTHES Research Group, RIKEN, Wako, Saitama 351-0198, Japan*

<sup>3</sup>*Astrophysics Research Centre, School of Mathematics and Physics, Queens University Belfast, Belfast, BT7 1NN, United Kingdom*

<sup>4</sup>*Monash Centre for Astrophysics, School of Physics and Astronomy, Monash University, VIC 3800, Australia*

<sup>5</sup>*Max-Planck-Institut für Astrophysik, Karl-Schwarzschild-Str. 1, D-85748 Garching, Germany*

<sup>6</sup>*University of Minnesota, School of Physics and Astronomy, Minneapolis, MN 55455, USA*

<sup>7</sup>*Shanghai Jiao-Tong University, Department of Physics and Astronomy, Shanghai 200240, P. R. China*

## ABSTRACT

We examine the nucleosynthesis in the innermost, neutrino-processed ejecta (a few  $10^{-3} M_{\odot}$ ) of self-consistent, two-dimensional explosion models of core-collapse supernovae for six progenitor stars with different initial masses. Three models have initial masses near the low-mass end of the supernova range,  $8.8 M_{\odot}$  (e8.8; electron-capture supernova),  $9.6 M_{\odot}$  (z9.6), and  $8.1 M_{\odot}$  (u8.1), with initial metallicities of 1, 0, and  $10^{-4}$  times the solar metallicity, respectively. The other three are solar-metallicity models with initial masses of  $11.2 M_{\odot}$  (s11),  $15 M_{\odot}$  (s15), and  $27 M_{\odot}$  (s27). The low-mass models e8.8, z9.6, and u8.1 exhibit high production factors (nucleosynthetic abundances relative to the solar ones) of 100–200 for light trans-iron elements from Zn to Zr. This is associated with appreciable ejection of neutron-rich matter in these models. Remarkably, the nucleosynthetic outcomes for progenitors e8.8 and z9.6 are almost identical, including interesting productions of  $^{48}\text{Ca}$  and  $^{60}\text{Fe}$ , irrespective of their quite different (O-Ne-Mg and Fe) cores prior to collapse. In the more massive models s11, s15, and s27, several proton-rich isotopes of light trans-iron elements, including the  $p$ -isotope  $^{92}\text{Mo}$  (for s27) are made, up to production factors of  $\sim 30$ . Both electron-capture and core-collapse supernovae near the low-mass end can therefore be dominant contributors to the Galactic inventory of light trans-iron elements from Zn to Zr and probably  $^{48}\text{Ca}$  and live  $^{60}\text{Fe}$ . The innermost ejecta of more massive supernovae may have only sub-dominant contributions to the chemical enrichment of the Galaxy except for  $^{92}\text{Mo}$ .

*Keywords:* nuclear reactions, nucleosynthesis, abundances — stars: abundances — stars: neutron — supernovae: general

## 1. INTRODUCTION

Core-collapse supernovae (CCSNe), the deaths of stars with initial masses heavier than about  $8M_{\odot}$ , have long been suggested to be important astrophysical sources of trans-iron species as well as of intermediate-mass and iron-group elements. Traditionally, studies of CCSN nucleosynthesis were based on artificial one-dimensional (1D) explosion models with free parameters such as the mass-cut (location of ejecta-remnant interface), the electron fraction ( $Y_e$ ; number of protons per nucleon) of the ejecta, and the explosion energy (e.g., Woosley & Weaver 1995; Thielemann 1996; Rauscher et al. 2002; Limongi & Chieffi 2006; Tominaga 2007; Heger & Woosley 2010; Nomoto et al. 2013). Nucleosynthetic abundances made near the mass-cut in the innermost ejecta are, however, highly dependent on such free parameters. The approach of replacing the complex multi-dimensional dynamics of a neutrino-driven supernova (SN) with a piston or thermal bomb as an artificial explosion engine is likely to be problematic when it comes to studying the innermost ejecta. The reason is that the time evolution of the thermal and kinetic energy of a neutrino-driven explosion may not be represented well by any of these explosion approximations. This makes it difficult to predict nucleosynthesis of some iron-group and trans-iron (Zn and heavier) elements based on such parameterized models.

Recent work by Sukhbold et al. (2016) has advanced the 1D approach by adopting parameterized neutrino-powered explosion models. In their models the boundary conditions (e.g., proto-neutron star contraction and core luminosity) are set deep inside the proto-neutron star and the physical conditions of the innermost ejecta are obtained as a result of hydrodynamical computations (see also Fröhlich et al. 2006; Perego et al. 2015, for comparable approaches beyond piston and thermal bomb models in 1D). Similar to previous works, they found production of elements from B to Cu in reasonable agreement with the solar ratio (except for some elements that had other contributors such as low-mass stars and SNe Ia). They reported, however, a severe deficiency of light trans-iron elements from Zn to Zr, which had been explained in part by the weak  $s$ -process in previous studies (e.g., Woosley & Heger 2007). In addition, astrophysical sources of  $^{48}\text{Ca}$  (neutron-rich isotope of Ca),  $^{64}\text{Zn}$  (main isotope of Zn), and  $^{92}\text{Mo}$  ( $p$ -isotope) still remain unresolved, for which a rare class of SNe Ia (Meyer et al. 1996; Woosley 1997), hypernovae (Umeda & Nomoto 2002; Tominaga 2007) and neutron-rich nuclear equilibrium (Hoffman et al. 1996; Wanajo 2006), respectively, have been proposed as possible explanations. Note, however, that Sukhbold et al. (2016)

did not include neutrino-heated (but just shock-heated) ejecta in their analysis.

One of the fundamental problems in such 1D models is obviously the limitation of dimensionality. Among other things, they do not account for the spatial variations in electron fraction  $Y_e$ , entropy  $S$ , and ejection velocity that is seen in multi-dimensional CCSN models. Two-dimensional (2D) simulations with sophisticated neutrino transport therefore provide a much better basis for studying the nucleosynthesis in the innermost CCSN ejecta. Pruet et al. (2005, 2006) used the hydrodynamical trajectories of a  $15M_{\odot}$  CCSN (Buras et al. 2006) for nucleosynthesis and showed that interesting amounts of Sc, Zn, and light  $p$ -nuclei were formed in the innermost proton-rich ejecta (see also Fujimoto et al. 2011), while the contribution of neutron-rich ejecta appeared to be subdominant (Hoffman et al. 2007). This was an important step beyond previous CCSN nucleosynthesis studies, but the explosion, though neutrino-driven, was still induced artificially like the piston-induced or thermal-bomb explosions of the previous 1D approaches, i.e., the 2D explosion was not obtained in a fully self-consistent manner. Moreover, based on the superior treatment of the neutrino transport in our present models we can re-investigate the question of nucleosynthesis in the neutron-rich ejecta, in which light trans-iron species could be abundantly produced (e.g., Hoffman et al. 1996).

To our knowledge, the only extant study of nucleosynthesis based on a self-consistent multi-dimensional explosion model is the one by Wanajo et al. (2011a, 2013a,b), which is based on a 2D simulation of an  $8.8M_{\odot}$  electron-capture SN (ECSN; a sub-class of CCSNe arising from collapsing O-Ne-Mg cores, Nomoto 1987; Janka et al. 2008). They found appreciable production of trans-iron elements from Zn to Zr,  $^{48}\text{Ca}$ , and  $^{60}\text{Fe}$  (radioactive nuclei) in the innermost neutron-rich ejecta, a very different result from nucleosynthesis studies (Hoffman et al. 2008; Wanajo et al. 2009) based on the corresponding 1D models (Kitauro et al. 2006; Janka et al. 2008). This demonstrates the importance of self-consistent multi-D models for reliable nucleosynthesis predictions.

2D explosion models only provide a first glimpse at the role of multi-D effects in supernova nucleosynthesis, however. Recent three-dimensional (3D) core-collapse simulations have shown qualitative and quantitative differences to 2D (see, e.g., Janka et al. 2016, for a recent review) concerning shock revival (with a trend towards delayed or missing explosions) and also concerning the multi-D flow dynamics and energetics during the first phase of the explosion (Melson et al. 2015; Müller 2015).

**Table 1.** Parameters of Supernova Explosion Models

Model	$M_{\text{prog}}^{\text{a}}$	$Z_{\text{prog}}^{\text{b}}$	$\Delta\theta^{\text{c}}$	$t_{\text{expl}}^{\text{d}}$	$t_{\text{fin}}^{\text{e}}$	$E_{\text{diag}}^{\text{f}}$
	( $M_{\odot}$ )	( $Z_{\odot}$ )	deg	(ms)	(ms)	( $10^{50}$ erg)
e8.8	8.8	1	1.4	92	362	0.9
z9.6	9.6	0	1.4	125	1420	0.6
u8.1	8.1	$10^{-4}$	1.4	177	335	0.4
s11 <sup>g</sup>	11.2	1	2.8	213	922	0.4
s15 <sup>h</sup>	15	1	2.8	569	779	1.3
s27 <sup>i</sup>	27	1	1.4	209	790	1.9

<sup>a</sup> Progenitor mass at the zero-age main sequence.<sup>b</sup> Metallicity at the zero-age main sequence.<sup>c</sup> Angular resolution.<sup>d</sup> Post-bounce time of explosion, defined as the point in time when the average shock radius ( $r_{\text{sh}}$ ) reaches 400 km.<sup>e</sup> Final post-bounce time reached in simulation.<sup>f</sup> Diagnostic explosion energy at the end of simulation.<sup>g</sup> Same as model s11.2 in Woosley et al. (2002) and Müller et al. (2012a).<sup>h</sup> Same as model s15s7b2 in Woosley & Weaver (1995) and Müller et al. (2012a).<sup>i</sup> Same as model s27.0 in Woosley et al. (2002) and Müller et al. (2012b).**Table 2.** Properties of Innermost SN Ejecta

Model	Type	$M_{\text{PNS}}^{\text{c}}$	$M_{\text{ej}}^{\text{d}}$	$M_{\text{ej,n}}^{\text{e}}$	$Y_{\text{e,min}}^{\text{f}}$	$Y_{\text{e,max}}^{\text{g}}$	$S_{\text{min}}^{\text{h}}$	$S_{\text{max}}^{\text{i}}$
		( $M_{\odot}$ )	( $10^{-3} M_{\odot}$ )	( $10^{-3} M_{\odot}$ )			( $k_{\text{B}} \text{ nuc}^{-1}$ )	( $k_{\text{B}} \text{ nuc}^{-1}$ )
e8.8	ECSN	1.36	11.4	5.83	0.398	0.555	9.80	383
z9.6	CCSN	1.36	12.4	4.94	0.373	0.603	12.6	27.8
u8.1	CCSN	1.36	7.69	3.24	0.399	0.612	9.83	29.9
s11	CCSN	1.36	14.1	0.133	0.474	0.551	6.64	34.7
s15	CCSN	1.58	15.9	0.592	0.464	0.598	6.78	36.7
s27	CCSN	1.65	27.3	0.759	0.387	0.601	5.19	44.0

<sup>c</sup> Baryonic mass of the proto-neutron star at the end of simulation.<sup>d</sup> Total mass in the innermost ejecta.<sup>e</sup> Ejecta mass with  $Y_{\text{e}} < 0.4975$ .<sup>f</sup> Minimal  $Y_{\text{e}}$  evaluated at  $T_9 = 10$  (see text).<sup>g</sup> Maximal  $Y_{\text{e}}$  evaluated at  $T_9 = 10$  (see text).<sup>h</sup> Minimal asymptotic entropy (at the end of simulation).<sup>i</sup> Maximal asymptotic entropy (at the end of simulation).

Thus, nucleosynthesis studies based on 3D models will eventually be needed, but are, of course, computationally much more demanding.

This paper aims at extending the 2D studies of Wanajo et al. (2011a, 2013a,b) to examine the nucleosynthesis in the innermost ejecta of CCSNe arising from iron-core progenitors. This will be an important step toward future nucleosynthesis studies from self-consistent 3D explosion models. In addition to the ECSN model studied by Wanajo et al. (2011a, 2013a,b), we consider five CCSN models with zero-age main sequence progenitor masses of  $9.6 M_{\odot}$  (initial metallicity of  $Z = 0 Z_{\odot}$ ),  $8.1 M_{\odot}$  ( $10^{-4} Z_{\odot}$ ), and  $11.2 M_{\odot}$ ,  $15 M_{\odot}$ , and  $27 M_{\odot}$  ( $1 Z_{\odot}$ ) (§ 2). By including the  $8.1 M_{\odot}$  and  $9.6 M_{\odot}$  progenitors side-by-side with an ECSN model, our study retains a strong focus on the low-mass end of the progenitor spectrum. With the uncertainties surrounding the ECSN channel (Poelarends et al. 2008; Jones et al. 2013, 2014; Doherty et al. 2015; Jones et al. 2016), one particular question that we seek to answer is whether ECSN-like nucleosynthesis can also be obtained for slightly different progenitor channels close to the iron core formation limit.

All these SN explosions were obtained self-consistently, i.e., with no free parameters, in 2D axisymmetric simulations adopting an elaborate neutrino transport scheme (Müller et al. 2012a,b; Janka et al. 2012). Nucleosynthetic abundances are calculated by applying an up-to-date reaction network code to hydrodynamic trajectories in a post-processing step (§ 3). Some details of the nucleosynthesis mechanisms operating in the innermost ejecta are described by taking the result of the metal-free  $9.6 M_{\odot}$  star as representative of our models. The mass-integrated nucleosynthetic yields are compared to the solar abundances to test if the innermost ejecta of these SNe can be major sources of light trans-iron elements and some other species in the Galaxy (§ 4). Our conclusions follow (§ 5).

## 2. SN MODELS

### 2.1. Numerical methods and progenitor models

All the SN hydrodynamical trajectories have been computed from 2D general relativistic simulations with energy-dependent ray-by-ray-plus neutrino transport based on a variable Eddington factor technique as implemented in the supernova code VERTEX (Rampp & Janka 2002; Buras et al. 2006; Müller et al. 2010). Except for the pseudo-relativistic ECSN model of Wanajo et al. (2011a), general relativity is treated in the extended conformal flatness approximation (Cordero-Carrión et al. 2009). A modern set of neutrino interaction rates (the “full rates” set of Müller et al. 2012a) has been

used for the simulations. The explosions were obtained self-consistently and thus the models contained no free parameters.

The initial pre-SN models were adopted from Nomoto (1987,  $8.8 M_{\odot}$  star with an O-Ne-Mg core with solar metallicity), A. Heger (unpublished<sup>1</sup>,  $9.6 M_{\odot}$  and  $8.1 M_{\odot}$  models<sup>2</sup> with metallicities  $Z = 0$  and  $Z = 10^{-4} Z_{\odot}$ , respectively), Woosley et al. (2002,  $11.2 M_{\odot}$  solar metallicity model, s11.2 in their paper), Woosley & Weaver (1995,  $15 M_{\odot}$  solar metallicity model, s15s7b2 in their paper), Woosley et al. (2002,  $27 M_{\odot}$  solar metallicity model, s27.0 in their paper). The corresponding explosion models are labeled as e8.8, z9.6, u8.1, s11, s15, and s27 hereafter. Relevant model parameters are summarized in Table 1. For more details on the individual explosion models, we refer the reader to the original publications on e8.8 (Wanajo et al. 2011a), z9.6 (Janka et al. 2012), u8.1 (Müller et al. 2012b), s11, s15s7b2 (Müller et al. 2012a), and s27 (Müller et al. 2012b).

Note that although we include two models of subsolar metallicity, the limited number of models does not permit us to discuss the dependency on metallicity in this paper.

### 2.2. Explosion dynamics

Snapshots of the electron fraction,  $Y_e$ , and the entropy per nucleon,  $S$ , in these simulations at late times are shown in Figure 1. One can see roughly spherical structures for e8.8 and z9.6 (top panels) and more strongly asymmetric features with a dipolar or quadrupolar geometry for the other models (middle and bottom panels). The different explosion dynamics reflects the core structures of pre-SN stars with steeper to shallower density gradients in the order of e8.8, z9.6, u8.1, s11, s15, and s27 (see Fig. 8 in Janka et al. 2012). The ECSN progenitor for e8.8 is a super-asymptotic giant branch (SAGB) star with an O-Ne-Mg core surrounded by a very dilute H-He envelope, while those of CCSNe are iron cores embedded by dense oxygen-silicon shells. For e8.8, therefore, the explosion sets in very early at a post-bounce time of  $t_{\text{pb}} \sim 80$  ms before vigorous convection can develop. Overturn driven by the Rayleigh-Taylor instability only occurs when the explosion is underway, but the plumes do not have sufficient time to merge into large structures so that no global asymmetry emerges. For the CCSN cases (except for z9.6), by contrast, the

<sup>1</sup> Extension of Heger & Woosley (2010).

<sup>2</sup> Both the  $9.6 M_{\odot}$  of zero metallicity and the  $8.1 M_{\odot}$  model of  $10^{-4} Z_{\odot}$  were at the low-mass ends of CCSN progenitors for their respective metallicities in the KEPLER calculations. See also Ibeling & Heger (2013) for general metallicity dependence of the CCSN lower mass limit.

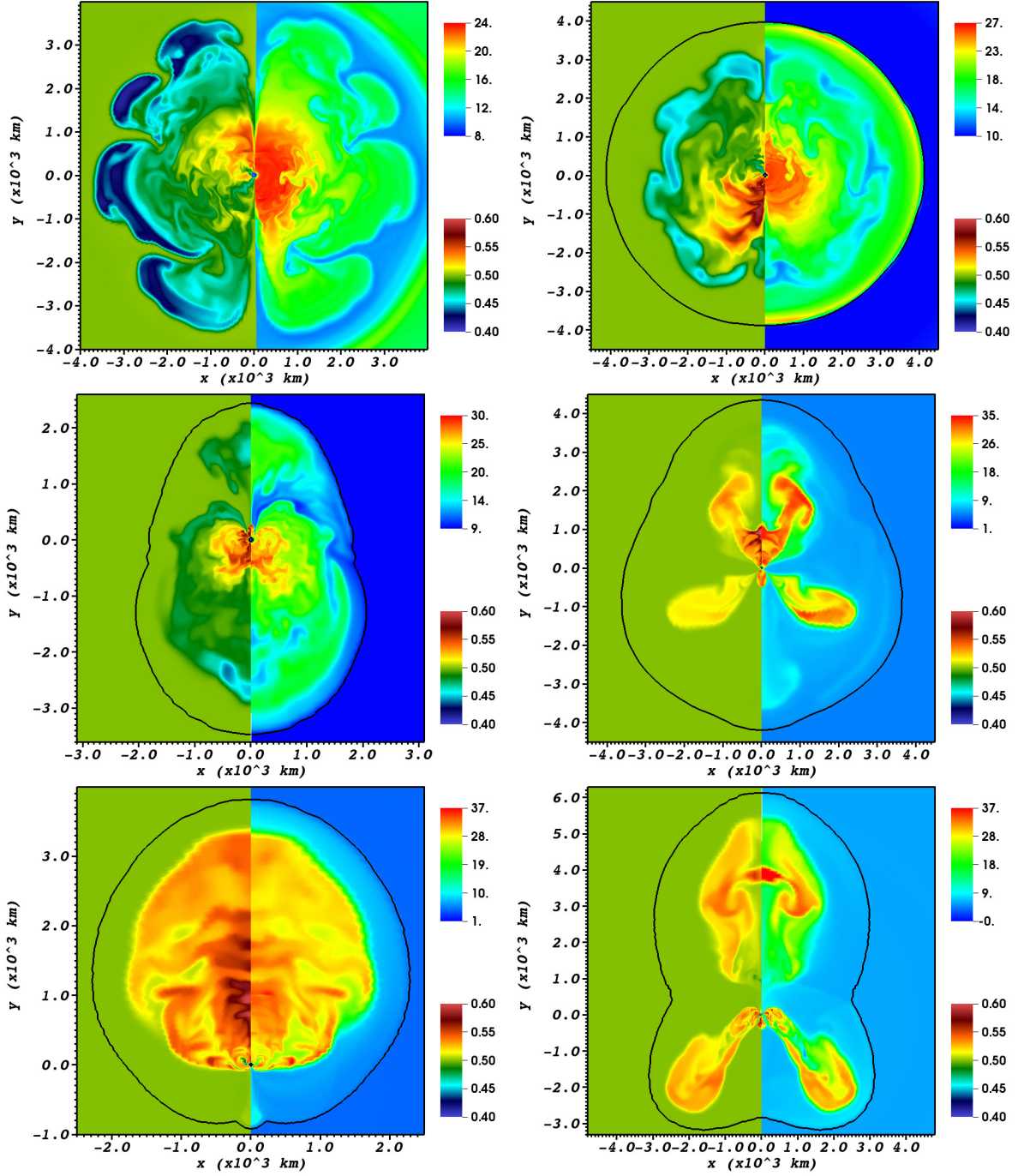


**Figure 1.** Late-time snapshots of models e8.8 (left-top, 266 ms after bounce), z9.6 (right-top, 317 ms), u8.1 (left-middle, 315 ms), s11 (right-middle, 922 ms), s15 (left-bottom, 776 ms), and s27 (right-bottom, 790 ms). Each panel shows the distribution of electron fraction,  $Y_e$  (left halves of panels; color-bar at right-bottom), and entropy per nucleon,  $S$ , in units of  $k_B/\text{nucleon}$  (right; color-bar at right-top) at a time when the high-entropy plumes of neutrino-heated matter have reached a radius of roughly 3000 km. The black line in each panel indicates the shock front. The vertical and horizontal axes show the distance from the center. Note that the shock has already propagated well beyond 4000 km in e8.8 at this stage and is therefore no longer visible in the plot.



explosions gradually start after multi-dimensional effects, i.e., convection or the standing-accretion-shock instability (SASI, Blondin et al. 2003), have reached the non-linear regime (the onset of the explosion occurs at  $t_{\text{pb}} \sim 500$  ms for s15 and  $t_{\text{pb}} \sim 150 \dots 200$  ms for the others, Table 1 and Fig. 14 in Janka et al. (2012)). Moreover, due to the presence of a relatively dense and massive oxygen shell, shock expansion is slow enough for a dominant unipolar or bipolar asymmetry to emerge after shock revival.

Models z9.6 and u8.1 stand apart from the more massive CCSN models s11, s15, and s27, since stars close to the iron core formation limit exhibit evolutionary and structural similarities to ECSN progenitors (Jones et al. 2013, 2014; Woosley & Heger 2015). Specifically, these progenitors have very thin O and C shells between the core and the low-density He and H envelope. Because of these peculiarities, model z9.6 (and to some degree u8.1) is a case on the borderline to ECSN-like explosion behavior. Its progenitor exhibits the steepest core-density gradient near the core-envelope interface among the CCSN cases, resulting in  $Y_e$  and  $S$  structures of the innermost ejecta rather similar to those of e8.8. The progenitor of u8.1 has a slightly shallower core-density gradient than that of z9.6 so that the propagation of the shock is slightly slower than for z9.6, but still faster than for typical iron-core progenitors. Since the width of the ECSN channel is subject to considerable uncertainties (see Poelarends et al. 2008; Jones et al. 2013, 2014; Doherty et al. 2015; Jones et al. 2016, and references therein), CCSNe from this mass range are particularly interesting as a possible alternative source for “ECSN-like” nucleosynthesis.

As in Wanaajo et al. (2011a) and similar to Wongwathanarat et al. (2016), we compute the trajectories for our nucleosynthesis calculations from the 2D data files (with a time spacing of 0.25 ms) instead of co-evolving tracer particles during the simulation. In order not to follow the tracers during multiple convective overturns with the risk of accumulating discretization errors, we integrate the tracer trajectories *backwards* in time from an appropriate point during the simulation (i.e., starting either from the end of the simulation, or from a time when the bulk of the ejecta have cooled sufficiently as in the case of z9.6). This procedure greatly reduces the number of required trajectories to adequately sample the ejecta: Selecting the final locations of the tracer particles only within the region of interest reduces the total mass of ejecta that must be covered (less than  $0.03M_\odot$ ) and makes it easy to use higher mass resolution where it is most needed, i.e., in the neutrino-processed ejecta.

### 2.3. Nucleosynthesis conditions in the ejecta

Some nucleosynthesis-relevant properties for all SN models are summarized in Table 2. It is important to note that we only calculate the nucleosynthesis for the “early ejecta”, i.e., consider only the material that has been ejected in neutrino-driven outflows or undergone explosive burning in the shock by the end of the simulations. The contributions of the outer shells and later neutrino-driven ejecta to the total yields are neglected.

For models e8.8, z9.6, and u8.1, explosive burning is already complete at the end of the simulations, and the outer shell (composed of H and He) will not add significant yields of heavy elements. We still miss small amounts of ejected material from the neutrino-driven wind in these progenitors, however. This material may undergo weak  $r$ - or  $\nu p$ -process nucleosynthesis, though the most recent calculations of wind nucleosynthesis for e8.8 suggest only a relatively unspectacular production of iron group elements and some  $\nu p$ -process nuclides with small production factors (Pillumbi et al. 2015), which turn out to be insignificant compared to the contribution from the early ejecta that we investigate here. For e8.8, z9.6, and u8.1, the yields presented here thus cover essentially the complete nucleosynthesis of heavy elements in these progenitors.

The case is different for s11, s15, and s27, where the shock has progressed only to the middle of the O/Si shell. For these models, substantial amounts of ashes from O, Ne, C, and He burning thus remain to be ejected and will contribute significantly to the total production factors. The post-shock temperatures at the end of our simulations also remain sufficiently high for some additional explosive O burning to take place. Moreover, strong accretion downflows still persist in these models. This keeps the neutrino luminosities high and allows the ejection of neutrino-heated matter to continue well beyond 1 s after the onset of the explosion (Müller 2015; Bruenn et al. 2016). Our nucleosynthesis calculations therefore place only a lower bound on the production of iron-group and trans-iron group elements in the supernova core of these models. It is noteworthy that this may partly contribute to the unexpectedly small mass of  $^{56}\text{Ni}$  obtained for these models, which remains significantly smaller than expected for “ordinary” supernovae (e.g.,  $0.07 M_\odot$  for SN 1987A, Bouchet et al. 1991).

Aside from the limitation of our analysis to the nucleosynthesis during the first few hundred milliseconds after shock revival, the nucleosynthesis in our models remains subject to other uncertainties: The simulations were conducted assuming axisymmetry (2D), and the explosion energies at the end of simulations are only  $(0.3\text{--}1.5) \times 10^{50}$  erg (see Fig. 15 in Janka et al. 2012),

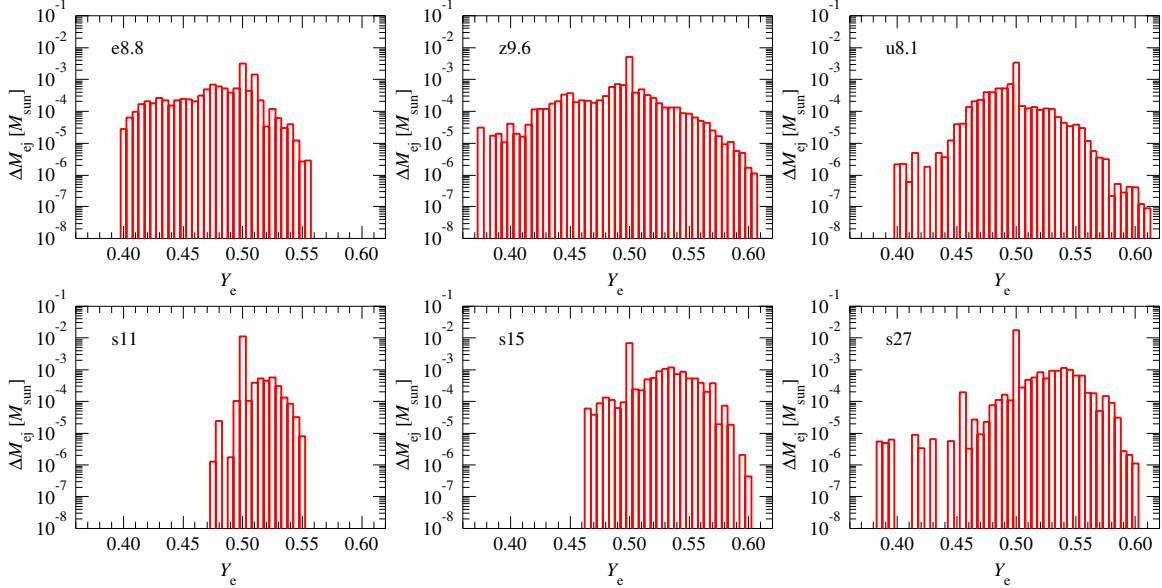


**Figure 2.**  $Y_e$  histograms for the SN ejecta when the temperatures have decreased to  $T_9 = 10$ . The ejecta masses ( $\Delta M_{\text{ej}}$ ) are shown as functions of  $Y_e$  with a bin size of  $\Delta Y_e = 0.005$ .

which are either less energetic than typical observed events (several  $10^{50}$  erg, e.g., Kasen & Woosley 2009; Nomoto et al. 2013) or still in a phase of steep rise, i.e., not converged to their final values. We discuss the possible repercussions of this in § 4.8 and § 5.

Figure 2 shows the  $Y_e$  distributions in the ejecta for all models evaluated at  $T_9 = 10$ , where  $T_9$  is the temperature in units of  $10^9$  K. For a trajectory with the maximum temperature of  $T_{9,\text{max}} < 10$ , we show  $Y_e$  at  $T_9 = T_{9,\text{max}}$  instead.  $\Delta M_{\text{ej}}$  is the ejecta mass in each  $Y_e$  bin with an interval of  $\Delta Y_e = 0.005$ . The minimum and maximum values of  $Y_e$  for all models are given in Table 2 (8th and 9th columns, respectively). The  $Y_e$  distributions shown here are similar to those inferred from the hydro data at late times except for small (up to a few %) shifts toward  $Y_e \approx 0.5$  as a result of some numerical diffusion and mixing (clipping of extrema) that suppresses the tails of the  $Y_e$  distribution in the hydro at late times<sup>3</sup>. We find that low-mass models (e8.8, z9.6, and u8.1) have appreciable amounts of neutron-rich ejecta (40–50%; 7th column in Table 2). This is due to the faster growth of the shock radii for these low-mass cases: As a result of the higher ejecta speed, less time is available to increase the  $Y_e$  by neutrino processing as material is ejected from the neutron-rich environment near the gain radius. By contrast, the bulk of the ejecta are proton-rich (96–99%; Table 2) in massive models

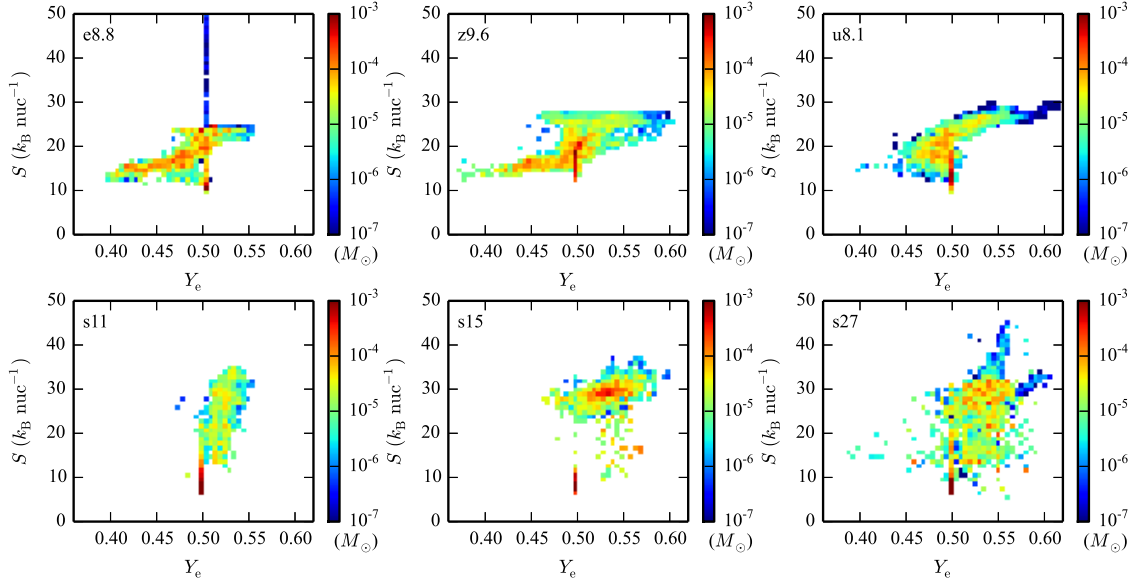
(s11, s15, and s27) because of the slower expansion of the ejecta.

Figure 3 illustrates the distributions of ejecta masses as functions of  $Y_e$  and asymptotic entropy per nucleon,  $S$  (in units of Boltzmann’s constant  $k_B$ ). All SN models show spikes of  $Y_e \approx 0.50$  components as leftovers of the initial composition of shocked material that never undergoes strong neutrino processing, and a positive correlation of  $S$  with  $Y_e$  in the neutrino-processed ejecta. The latter fact is reasonable because neutrino-heating raises both  $Y_e$  and  $S$ . We find, however, a larger scatter of the entropies at a given  $Y_e$  for massive SN models (s11, s15, and s27). This reflects the more vigorous motions arising from convective instability and SASI for more massive cases as well as stronger temporal and spatial variations in the neutrino irradiation.

Note that the very high entropies at  $Y_e \approx 0.5$  for e8.8 (up to  $S_{\text{max}} = 383k_B$ ; last column in Table 2) stem from shock heating of outgoing material colliding with the dilute SAGB envelope. However, a sizable post-shock entropy,  $S > 100k_B$ , is reached only in shells which never reach nuclear equilibrium ( $T_9 < 3$ , Janka et al. 2008; Kuroda et al. 2008) so that these shells do not contribute to the production of heavy elements (such as an  $r$ -process suggested by Ning et al. 2007). Except for this component of shock-heated ejecta with low temperatures, e8.8 has a maximum entropy of nucleosynthesis-relevant material of  $\approx 25k_B$ , and more massive models have larger values ( $S_{\text{max}}$ ; last column in Table 2).

The core-collapse simulations were stopped at  $t = t_{\text{fin}}$  for our models, where  $t_{\text{fin}} = 0.423$  s, 0.605 s, 0.474 s, 0.767 s, 0.947 s, and 1.13 s after core bounce for e8.8,

<sup>3</sup> In practice, we find this effect to be small up to the point where the ejecta reach a radius of around 1000 km and the radial computational grid becomes coarser.



**Figure 3.** Distributions of ejecta masses as functions of electron fraction ( $Y_e$ ) and asymptotic entropy per nucleon ( $S$ ) for all SN models. Strongly neutrino-processed ejecta show a wide range of  $Y_e$ -values and a slightly positive correlation between  $S$  and  $Y_e$ . Material that is shocked at relatively large radii after the onset of the explosion appears in the form of a narrow vertical stripe with  $Y_e \approx 0.5$  in the plots and exhibits variations in  $S$  depending on the pre-shock entropy and density and the shock velocity.

z9.6, u8.1, s11, s15, and s27, respectively. At these times, the temperatures in the ejecta were still high, in particular for massive models, so that nucleosynthesis would be still active. The temperature ( $T$ ) and density ( $\rho$ ) thus need to be extrapolated for nucleosynthesis calculations. It is known that the late-time evolution of the density is well approximated by  $\rho \propto t^{-2}$  (e.g., Arcones et al. 2007). We thus assume

$$\rho(t) = c_1(t - t_1)^{-2} \quad (t > t_{\text{fin}}), \quad (1)$$

where the constants  $c_1$  and  $t_1$  are determined to get a smooth connection of the density at  $t = t_{\text{fin}}$ . The expansion of the ejecta is almost adiabatic at this stage (i.e.,  $T^3/\rho \approx \text{constant}$ )<sup>4</sup>, and thus the temperature is extrapolated such as

$$T(t) = c_2(t - t_1)^{-2/3} \quad (t > t_{\text{fin}}) \quad (2)$$

with  $t_1$  from Equation (1) and  $c_2$  determined so that the temperature matches the value at  $t = t_{\text{fin}}$ . The radius  $r$  for  $t > t_{\text{fin}}$ , which is needed to calculate the rates of neutrino interactions, is obtained from Equation (1) with the assumption of steady-state conditions,

<sup>4</sup> Entropy generation due to electron-positron annihilation after the freezeout from nuclear statistical equilibrium (NSE) is not taken into account for deriving Equation (2). We expect, however, that its effect is minor because of the strong dependencies of nucleosynthetic abundances on  $Y_e$  rather than entropy or expansion timescale.

i.e.,  $r^2 \rho v_r = \text{constant}$  (Panov & Janka 2009; Wanajo et al. 2011b), where  $v_r$  is the radial component of velocity at  $t = t_{\text{fin}}$  and constant afterwards.

### 3. NUCLEOSYNTHESIS

The nucleosynthesis yields in each SN trajectory are computed in a post-processing step by solving an extensive nuclear reaction network (Wanajo et al. 2001) with the temperature and density histories described in § 2. The numbers of processed trajectories are 2343 (e8.8), 6310 (z9.6), 4672 (u8.1), 2739 (s11), 2565 (s15), and 2312 (s27). The up-to-date network consists of 7435 isotopes between the proton- and neutron-drip lines from single neutrons and protons up to isotopes with  $Z = 110$ . All the reaction rates are taken from REACLIB V2.0<sup>5</sup> (Cyburt et al. 2010) making use of experimental data when available. As we will see later, the nucleosynthetic abundances are mostly determined in nuclear equilibrium in the regions relatively close to  $\beta$ -stability where experimental masses are available. Uncertainties arising from nuclear data are thus expected to be small. Rates for electron capture (Langanke & Martinez-Pinedo 2001) as well as for neutrino interactions on free nucleons (McLaughlin et al. 1996) and  $\alpha$ -particles (Woosley et al. 1990) are also included. The radiation field computed in the supernova simulations

<sup>5</sup> <https://groups.nsl.msu.edu/jina/reaclib/db/>.



is used as input for computing the neutrino interactions in our nucleosynthesis calculations. We fully retain the spatial dependence of the radiation field as computed in our ray-by-ray-plus approximation in this post-processing step, because we have stored the relevant neutrino quantities along with the tracer trajectories.

Each nucleosynthesis calculation is initiated when the temperature decreases to  $T_9 = 10$  with the initial mass fractions of  $1 - Y_e$  and  $Y_e$  for free neutrons and protons, respectively<sup>6</sup>. For the trajectories with  $T_{9,\text{max}} < 10$ , the initial compositions adopted from our hydrodynamical simulations are utilized.

### 3.1. Types of nucleosynthesis

We first analyze the nucleosynthesis in detail for z9.6, since this model covers the widest range in  $Y_e$  ( $Y_e=0.373\text{--}0.603$ ; Fig. 2). Figure 4 shows the neutron-, proton-, and  $\alpha$ -to-seed abundance ratios ( $Y_n/Y_h$ ,  $Y_p/Y_h$ , and  $Y_\alpha/Y_h$ ) at a point when the temperatures decrease to  $T_9 = 3$  for all the trajectories of model z9.6. We consider this temperature as it approximately corresponds to the end of nuclear equilibrium: This temperature is close to the conventional critical temperature for the termination of quasi-nuclear equilibrium (QSE;  $T_9 = 4$ , Meyer et al. 1998b), to the beginning of a  $\nu p$ -process ( $T_9 = 3$ , Fröhlich et al. 2006), and the beginning of an  $r$ -process ( $T_9 = 2.5$ , Woosley et al. 1994). Here, the seed abundance  $Y_h$  is defined as the total abundance of all nuclei heavier than helium. The other SN models show similar dependencies of  $Y_n/Y_h$ ,  $Y_p/Y_h$ , and  $Y_\alpha/Y_h$  on  $Y_e$  (not shown here), indicating that  $Y_e$  (rather than entropy and expansion timescale) is most crucial for the nucleosynthesis in our case. For this reason, we describe our nucleosynthetic results for model z9.6 in terms of  $Y_e$ . According to Figure 4, we can distinguish the following three different types of nucleosynthesis regimes in our supernova models: A nuclear statistical equilibrium (NSE) regime for  $Y_e < 0.43$ , a quasi-nuclear equilibrium (QSE) regime for  $0.43 \leq Y_e < 0.5$ , and nucleosynthesis by charged-particle capture processes for  $Y_e \geq 0.5$ . No  $r$ -process is expected in our models because of neutron-to-seed ratios far below unity over the entire range of  $Y_e$  (Fig. 4).

#### 3.1.1. NSE

For  $Y_e < 0.43$ , all the ratios  $Y_n/Y_h$ ,  $Y_p/Y_h$ , and  $Y_\alpha/Y_h$  are considerably smaller than unity ( $< 0.01$ ) at  $T_9 = 3$  (Fig. 4). The global distribution of final nucleosynthetic

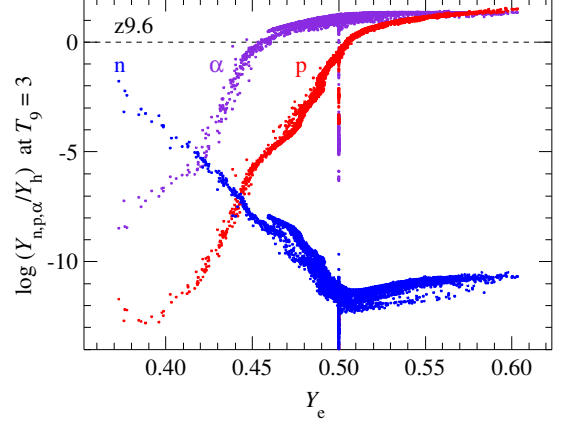


**Figure 4.** Neutron-, proton-, and  $\alpha$ -to-seed abundance ratios (blue, red, and purple, respectively) for all trajectories of z9.6 at a time when the temperatures decrease to  $T_9 = 3$  as functions of  $Y_e$  (at  $T_9 = 10$ ).

abundances is thus mostly determined in NSE at high temperature ( $T_9 > 5$ )<sup>7</sup>. The subsequent QSE does not substantially change the abundance distribution because of the small amounts of free nucleons and  $\alpha$  particles. This is due to relatively small entropies ( $S \sim 14 k_B/\text{nuc}$ ; Fig. 3) for these neutron-rich ejecta and the neutron-richness itself. Under such conditions the three-body process  $\alpha(\alpha n, \gamma)^9\text{Be}$  (followed by  $^9\text{Be}(\alpha, \gamma)^{12}\text{C}$ ), rather than triple- $\alpha$ , is fast enough to form the NSE cluster by assembling free nucleons and  $\alpha$  particles. Such neutron-rich conditions also disfavor  $\alpha$  emission (i.e., to avoid to be more neutron-rich). In NSE, the resulting abundance distribution is independent of specific reactions. What determines the abundance distribution are the binding energies per nucleon ( $B/A$ ; shown in Figure 5, left). As the  $Y_e$  of nuclides (indicated by white lines) decreases from  $\sim 0.50$  to  $\sim 0.40$ , the nuclides with the maximal  $B/A$  shift from  $^{56}\text{Ni}$  ( $Z = N = 28$ ) to  $^{48}\text{Ca}$  ( $Z = 20$  and  $N = 28$ ) and  $^{84}\text{Se}$  ( $Z = 34$  and  $N = 50$ , see Hartmann et al. 1985).

We find such NSE-like nucleosynthesis features in Figure 6, which shows the abundance distribution in selected trajectories of model z9.6 when the temperatures decrease to  $T_9 = 5$ , 4, and 3 as well as the abundances at the end of calculations. The top three panels correspond to the trajectories with NSE-like conditions of  $Y_e < 0.43$  and relatively low entropies ( $\sim 14 k_B/\text{nuc}$ ). Major abundance peaks are already formed at  $T_9 = 5$  (red lines). The abundance patterns are almost frozen

<sup>6</sup> At such high temperature (and density), the matter immediately attains nuclear statistical equilibrium (NSE) and thus any initial composition with the total charge of  $Y_e$  is available.

<sup>7</sup> In this paper, we use the term “NSE” even for the case of  $\alpha$ -deficient QSE (Meyer et al. 1996; Wanajo et al. 2013a), in which NSE serves as a reasonable guideline for abundance determinations.

when the temperature decreases to  $T_9 = 4$  (defined as the end of NSE) and do not change significantly during the subsequent evolution.

### 3.1.2. QSE

For  $0.43 \leq Y_e < 0.50$ , the  $\alpha$  concentration becomes important ( $Y_\alpha/Y_h \sim 0.01$ – $10$ ) but  $Y_p/Y_h$  is less than unity at  $T_9 = 3$ . In this case, the final abundances are mainly determined in QSE, a subsequent stage after the  $\alpha$ -rich freeze-out from NSE (Woosley & Hoffman 1992; Meyer et al. 1998b). At the end of NSE ( $T_9 \sim 5$ ), the single NSE cluster splits into two QSE clusters with one consisting of free nucleons and  $\alpha$  particles and the other consisting of heavy nuclei. In the latter QSE cluster, the heavy nuclei are absorbed in the “ $\alpha$ -bath” and its distribution is determined by the  $\alpha$  separation energies (shown in the right panel of Figure 5), independent of specific nuclear reactions. With a modest neutron-richness of  $Y_e \sim 0.43$ – $0.49$  (values are indicated by white lines in Fig. 5), the nuclides near  $N = 28$  and  $50$  such as  $^{64}\text{Zn}$ ,  $^{88}\text{Sr}$ ,  $^{89}\text{Y}$ ,  $^{90}\text{Zr}$ , and  $^{92}\text{Mo}$  are preferentially formed in QSE owing to their greater  $\alpha$  separation energies (see also Hoffman et al. 1996; Wanajo 2006).

We find in the left-middle and middle panels of Figure 6 ( $Y_e = 0.450$  and  $0.475$ , respectively) that the abundance distributions substantially change during QSE ( $T_9 \sim 5$  to  $4$ ). The abundance patterns are determined roughly when the temperature decreases to  $T_9 = 3$ , and further evolution are unimportant (although an enhancement of nuclei with  $A = 10$ – $50$  can be seen as a result of  $\alpha$ -particle capture).

### 3.1.3. Charged-particle capture process

For  $Y_e \geq 0.50$ ,  $^{56}\text{Ni}$  dominates in the heavy QSE cluster, and the  $\alpha$ -rich freeze-out from QSE ( $T_9 \sim 4$ ) leads to an  $\alpha$ -process (Woosley & Hoffman 1992). This greatly enhances the abundances of  $\alpha$ -elements with  $A \sim 12$ – $40$  (with multiples of 4) as can be seen in the right-middle panel of Figure 6 (for  $Y_e = 0.500$ ). For  $Y_e > 0.51$ , both  $Y_\alpha/Y_h$  and  $Y_p/Y_h$  are greater than unity at  $T_9 = 3$  (Fig. 4). The freeze-out is thus followed by  $\alpha$ -capture and proton-capture processes. We find in the bottom three panels of Figure 6 ( $Y_e = 0.525$ ,  $0.550$ , and  $0.603$ ) that nuclei in a wide range of  $A \sim 10$ – $70$ , including odd- $Z$  elements, are substantially enhanced by these charged-particle capture processes after the temperature drops below  $T_9 = 3$ .

Figure 7 compares the final abundances with (blue) and without (cyan) neutrino reactions for the trajectory that has the highest  $Y_e = 0.603$  in model z9.6 (same as that in the right-bottom panel of Fig. 6). This indicates that the enhancement of nuclei with  $A = 60$ – $70$  is due

to a  $\nu p$ -process, in which the faster  $(n, p)$  and  $(n, \gamma)$  reactions with the free neutrons supplied by  $\bar{\nu}_e$  capture on free protons replace the slower  $\beta^+$ -decays (Fröhlich et al. 2006; Pruet et al. 2006; Wanajo 2006). Note that the  $\nu p$ -process in our result is very weak and only the nuclei up to  $A \sim 70$  are produced despite its substantial proton-richness (up to  $Y_e = 0.603$ ). By contrast, Wanajo et al. (2011b) have shown that the  $\nu p$ -process in neutrino-driven wind with similar proton-richness can produce nuclei up to  $A \sim 120$  (see also Pruet et al. 2006; Arcones et al. 2012). This discrepancy is due to the lower entropies and longer expansion timescales in the early dynamical ejecta, which reduces  $Y_p/Y_h$  at the beginning of a  $\nu p$ -process ( $T_9 \sim 3$ ), than those in the late-time neutrino-driven wind.

### 3.2. Dependencies of isotope productions on $Y_e$

In § 3.1 we found that the iron-group (from Ca to Cu) and light trans-iron (from Zn to Mo) species can be produced in the innermost ejecta of z9.6, the model with the widest range in  $Y_e$  in the ejecta. No heavier elements are produced in any of our six models. In Figures 8 and 9, the final mass fractions of stable isotopes from K to Mo are presented as functions of  $Y_e$  for all the trajectories of model z9.6. The mass fractions of selected radioactive isotopes (before decay) are also shown in the right-bottom panel of Figure 9. We find from these figures that few isotopes exhibit maximum abundances near  $Y_e = 0.5$ , in particular the light trans-iron species (from Zn to Mo). Overall, Ni and light trans-iron species are predominantly formed in neutron-rich ejecta, although the weak  $\nu p$ -process in proton-rich ejecta plays a sub-dominant role for those up to Ge. Several isotopes such as  $^{48}\text{Ca}$ ,  $^{50}\text{Ti}$ ,  $^{54}\text{Cr}$ , and radioactive nuclide  $^{60}\text{Fe}$  are made only in very neutron-rich ejecta with  $Y_e \sim 0.40$ – $0.43$  (Wanajo et al. 2013a,b). This sensitivity clearly demonstrates the importance of nucleosynthesis studies based on multi-dimensional SN simulations with detailed multi-group neutrino transport, which are indispensable for accurately determining the  $Y_e$ -distribution in the ejecta.

## 4. CONTRIBUTION TO THE GALAXY

For each SN model, we calculate mass-integrated abundances from the nucleosynthetic outcomes of all trajectories.<sup>8</sup> In the following subsections, we discuss the possible contribution of products from the innermost ejecta of SNe to the Galaxy by comparing our nucleosynthesis yields to the solar values. In particular, we focus

<sup>8</sup> Tables of the nucleosynthesis yields for all the SN models are available from <http://cosnucs.riken.jp/download.html>.

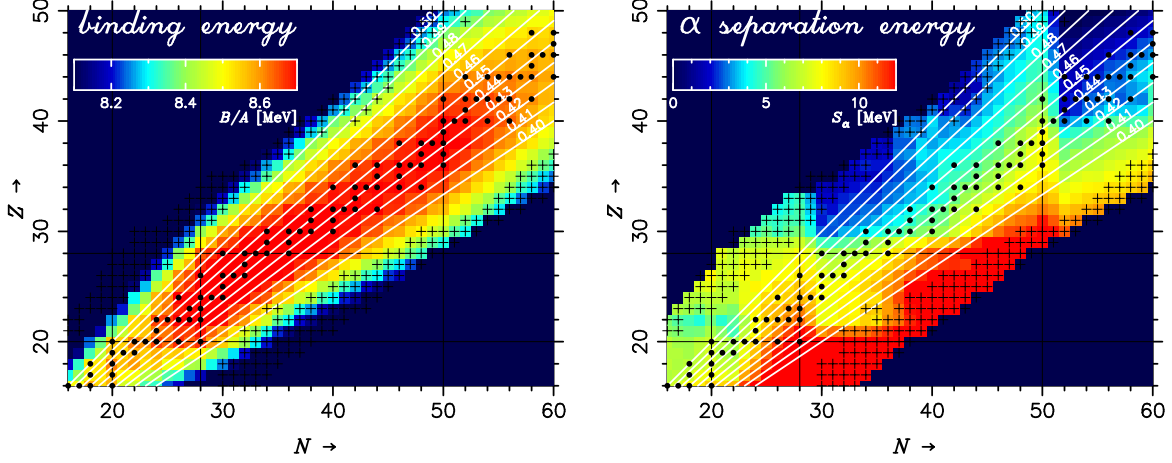


**Figure 5.** Binding energies per nucleon (left) and  $\alpha$ -separation energies (right) in units of MeV for nuclides with experimentally evaluated masses (crosses mark the extrapolated values, Audi et al. 2012). The dots denote stable isotopes. The black and white lines indicate neutron and proton magic numbers (20, 28, and 50) and the  $Y_e$  values of nuclides, respectively.

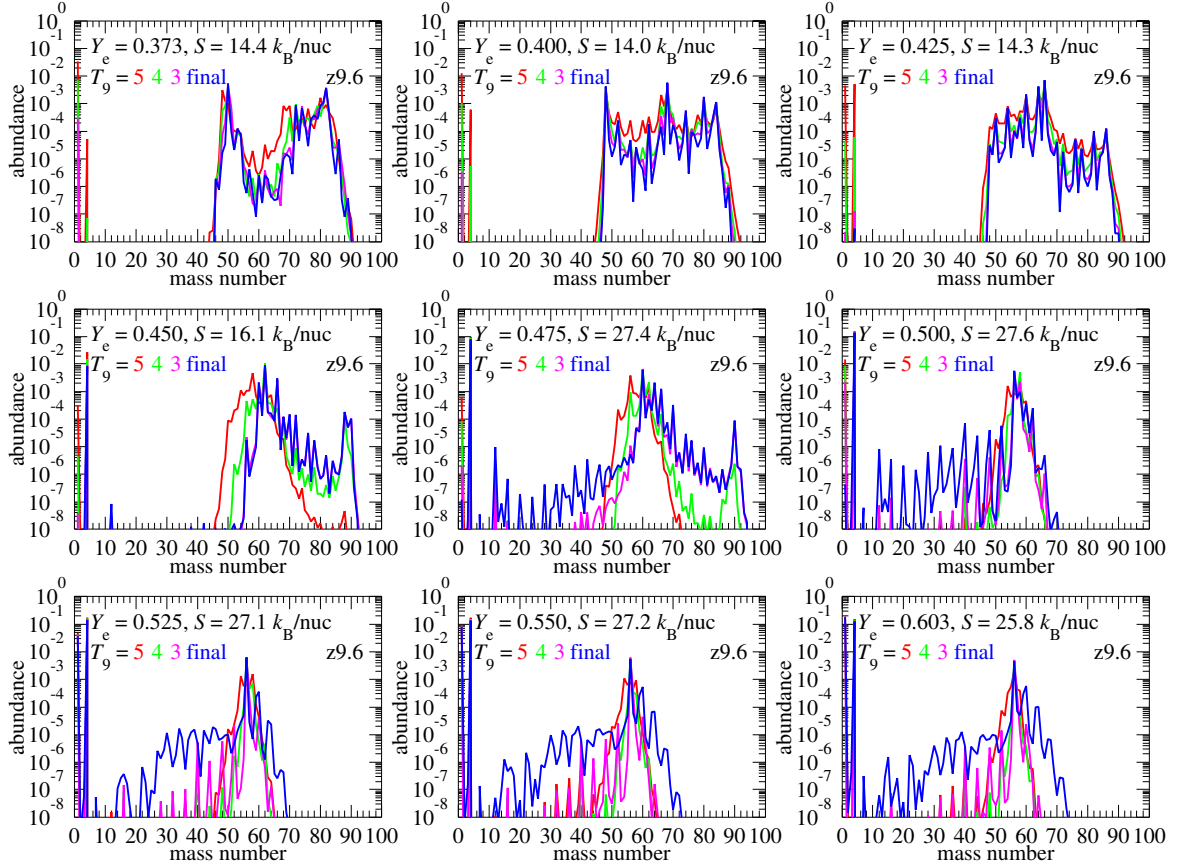


**Figure 6.** Nucleosynthetic abundances for model z9.6 when the temperatures decrease to  $T_9 = 5, 4$ , and  $3$  as well as those at the end of calculations (“final”). Selected trajectories are those with initial  $Y_e = 0.373$  (left-top),  $0.400$  (middle-top),  $0.425$  (right-top),  $0.450$  (left-middle),  $0.475$  (middle),  $0.500$  (right-middle),  $0.525$  (left-bottom),  $0.550$  (middle-bottom), and  $0.603$  (right-bottom). The asymptotic entropy  $S$  is also shown in the legend of each panel.

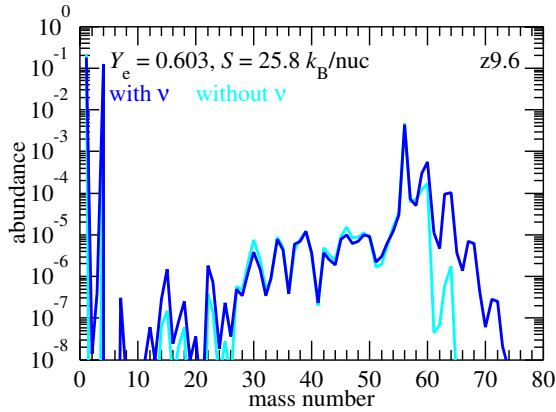


**Figure 7.** Same as the final abundance pattern in the right-bottom panel of Figure 6, but neglecting neutrino interactions below  $T_9 = 10$  (cyan).

on the production of several key species such as  $^{48}\text{Ca}$ , Zn isotopes, light trans-iron elements,  $p$ -nuclide  $^{92}\text{Mo}$ , and the radioactive isotopes  $^{56}\text{Ni}$  and  $^{60}\text{Fe}$ .

#### 4.1. Comparison with the elemental solar abundance

For all SN models, the mass-integrated yields are compared to the solar abundance (Lodders 2003). Figure 10 shows the elemental mass fractions in the total ejecta with respect to their solar values, i.e., “production factors”, for these models. The total ejecta mass from each SN is taken to be the sum of the ejected mass from the core and the outer envelope, that is,  $M_{\text{prog}} - M_{\text{PNS}}$  in Tables 1 and 2. Here, the outer envelope is assumed to be metal-free (i.e., H and He only), which is reasonable for the models near the low-mass end of the SN range, e8.8, z9.6, and u8.1. For the more massive models s11, s15, and s27, one should bear in mind that there is an important additional contribution to heavy elements (those heavier than helium) from the outer envelope (see Woosley et al. 2002; Woosley & Heger 2007, and references therein).

In each panel of Figure 10, we show a “normalization band” in yellow, which covers the range within 1 dex of the maximum production factor and one-tenth of that. The elements that reside in this band can be (at least in part) originate from SNe represented by each model, provided that their production factors are greater than  $\sim 10$  (e.g., Woosley & Heger 2007). As an order-of-magnitude estimate, the production factors of  $\sim 40$  for light trans-iron elements from Zn to Zr in our representative model z9.6 suggest that such low-mass CCSNe can be the major sources of these elements if these events account for a few 10% of all CCSNe and would still contribute sizable amounts if they make up  $\sim 10\%$  of all CCSNe. This suggests that SNe at the low-mass end of the progenitor spectrum as represented by mod-

els e8.8, z9.6, and u8.1 could be an important source of light trans-iron elements (§ 4.6).

Note that there is a remarkable agreement of the nucleosynthesis of z9.6 with that of e8.8, which is a consequence of the similarity of their pre-SN core structures with a steep density gradient outside the core and a very dilute outer envelope. In both cases, the resulting fast explosion lead to the ejection of appreciable amounts of neutron-rich material. Model u8.1 with a core structure very similar to (but with a slightly shallower density gradient than) that of z9.6 results in, however, a different nucleosynthetic trend with deficiencies of several elements between Zn and Zr. This indicates that only a slight difference of pre-SN core-density structures can lead to substantially different nucleosynthesis outcomes.

For more massive models, the production factors are smaller than  $\sim 10$  for all elements, despite their greater ejecta masses compared to low-mass models ( $M_{\text{ej}}$  in Table 2). The maximum production factor of  $\sim 1$  for s11 gives no element to be responsible for the Galactic chemical evolution. For s15 and s27, only Zr with the production factor  $\sim 10$  can be the elements that can be originated from these types of CCSNe. These SNe can be, however, possible contributors of some isotopes as discussed in § 4.2. Moreover, the non-neutrino processed “outer ejecta” from these stars, which are not fully included in our study, contribute significantly to the chemical enrichment of the Galaxy as discussed before.

#### 4.2. Comparison with the isotopic solar abundance

Figure 11 compares the isotopic abundances with the solar values for all SN models. The maximum isotopic production factor for each model is generally greater than that of elements (§ 4.1), and therefore places tighter constraints on the contribution of relevant SNe to the Galaxy. In Table 3, we list the 5 largest production factors for each model. Note that most of the isotopes listed here are made in nuclear equilibrium, and thus uncertainties in individual nuclear reaction rates are irrelevant. Models e8.8 and z9.6 exhibit appreciable production factors of 354 ( $^{86}\text{Kr}$ ) and 168 ( $^{82}\text{Se}$ ), respectively. This implies that such low-mass SNe account for  $\sim 10\%$  of all CCSN events (according to the reason described in § 4.1), supposing that these trans-iron elements originate solely from this class of events. A similar contribution of u8.1-like events can be expected with its largest production factor of 149 ( $^{74}\text{Se}$ ). The maximum production factor of 1.48 for s11 indicates that no species are dominantly produced in the innermost ejecta of such SNe. For s15 and s27, the largest production factors are 24.8 and 43.1 ( $^{74}\text{Se}$ ), respectively, which are sizably greater



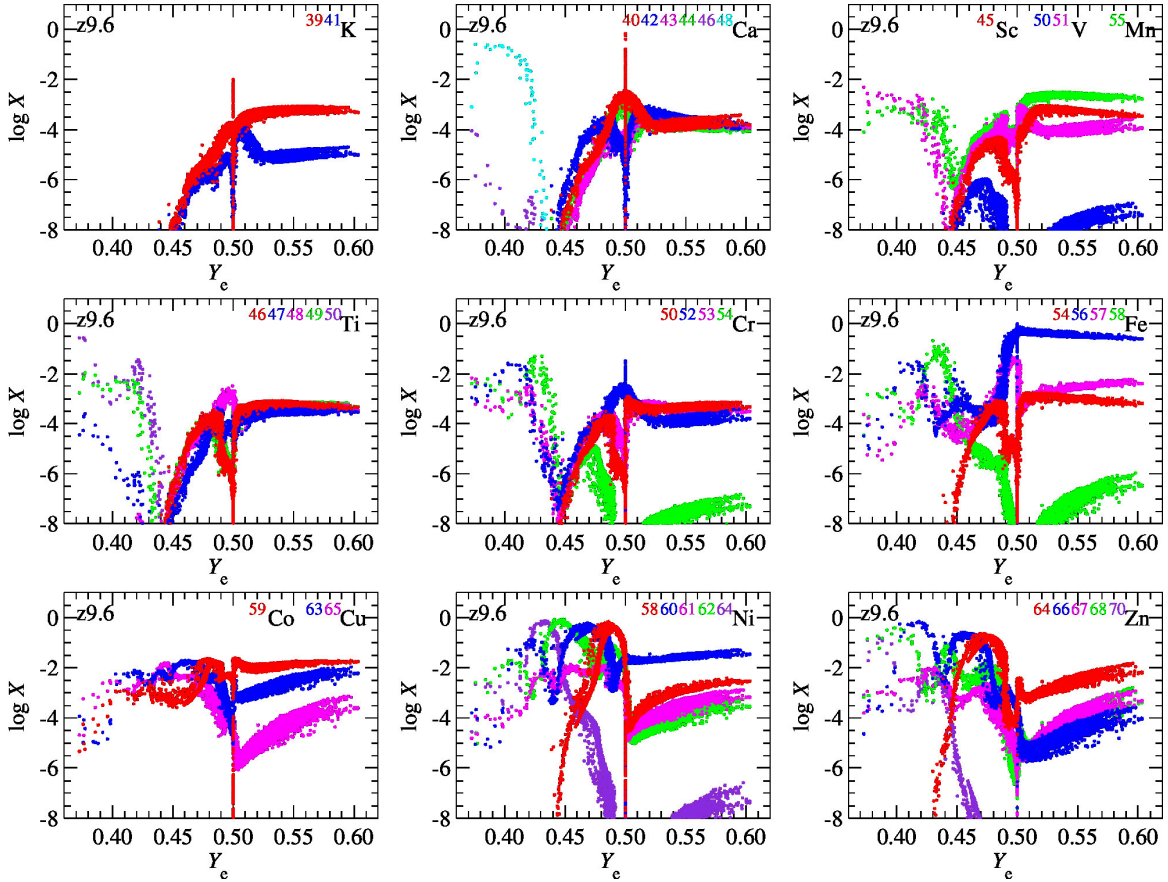


**Figure 8.** Final mass fractions (after  $\beta$ -decay) of the stable isotopes of K (left-top), Ca (middle-top), Sc, V, and Mn (right-top), Ti (left-middle), Cr (middle), Fe (right-middle), Co and Cu (left-bottom), Ni (middle-bottom), and Zn (right-bottom) as functions of  $Y_e$  for all the trajectories of model z9.6.

than those of elements ( $\sim 10$ , Fig. 11). This indicates that such intermediate-mass and massive CCSNe can be important sources of several species listed in Table 3.

To be more quantitative, we consider  $^{82}\text{Se}$  with the largest production factor for model z9.6 as representative. By assuming  $f_{z9.6}$  to be the fraction of z9.6-like events to all CCSNe, we have (Wanajo et al. 2011a)

$$\frac{f_{z9.6}}{1 - f_{z9.6}} = \frac{X_{\odot}(^{82}\text{Se})/X_{\odot}(^{16}\text{O})}{M_{z9.6}(^{82}\text{Se})/\langle M(^{16}\text{O}) \rangle} = 0.164, \quad (3)$$

where  $X_{\odot}(^{82}\text{Se}) = 1.38 \times 10^{-8}$  and  $X_{\odot}(^{16}\text{O}) = 6.60 \times 10^{-3}$  are the mass fractions in the solar system (Lodders 2003),  $M_{z9.6}(^{82}\text{Se}) = 1.91 \times 10^{-5} M_{\odot}$  is the ejecta mass of  $^{82}\text{Se}$  for z9.6, and  $\langle M(^{16}\text{O}) \rangle = 1.5 M_{\odot}$  is the production of  $^{16}\text{O}$  by massive CCSNe averaged over the stellar initial mass function between  $13 M_{\odot}$  and  $40 M_{\odot}$  (see Wanajo et al. 2009).<sup>9</sup> Equation (3) gives  $f_{z9.6} = 0.14$ , which corresponds to a mass window  $\Delta M_{\text{prog}} \sim 1 M_{\odot}$  near the low-mass end of the SN progenitor spectrum,

$M_{\text{prog}} \sim 9 M_{\odot}$ . It is currently uncertain whether this mass window for z9.6-like progenitors is reasonable or not, as only a slight difference of core-density structure leads to a very different nucleosynthetic result of u8.1. If we apply Equation (3) to model e8.8 by replacing  $^{82}\text{Se}$  with  $^{86}\text{Kr}$  (Table 3), we get  $f_{e8.8} = 0.085$ . This corresponds to a mass window of  $\Delta M_{\text{prog}} \sim 0.5 M_{\odot}$ , which is in reasonable agreement with the prediction from synthetic SAGB models at solar metallicity (Poelarends et al. 2008). It is thus well conceivable that a combination (or either) of ECSNe and low-mass CCSNe accounts for the production of light trans-iron species in the Galaxy. For the more massive models s11, s15, and s27, a lack of self-consistent nucleosynthesis yields in the outer envelopes precludes a quantitative estimate of their contributions.

#### 4.3. Neutron-rich vs. proton-rich ejecta

Our results described in § 4.1 and 4.2 shows that SNe near the low-mass end produce appreciable amounts of trans-iron species despite their small ejecta masses (compared to those of massive models;  $M_{\text{ej}}$  in Table 2). The reason can be found in Figure 12, which shows the frac-

<sup>9</sup> The value is in agreement with the estimated oxygen mass ( $1.4 \pm 0.7 M_{\odot}$ ) from SN 1987A (Fransson & Kozma 2006).



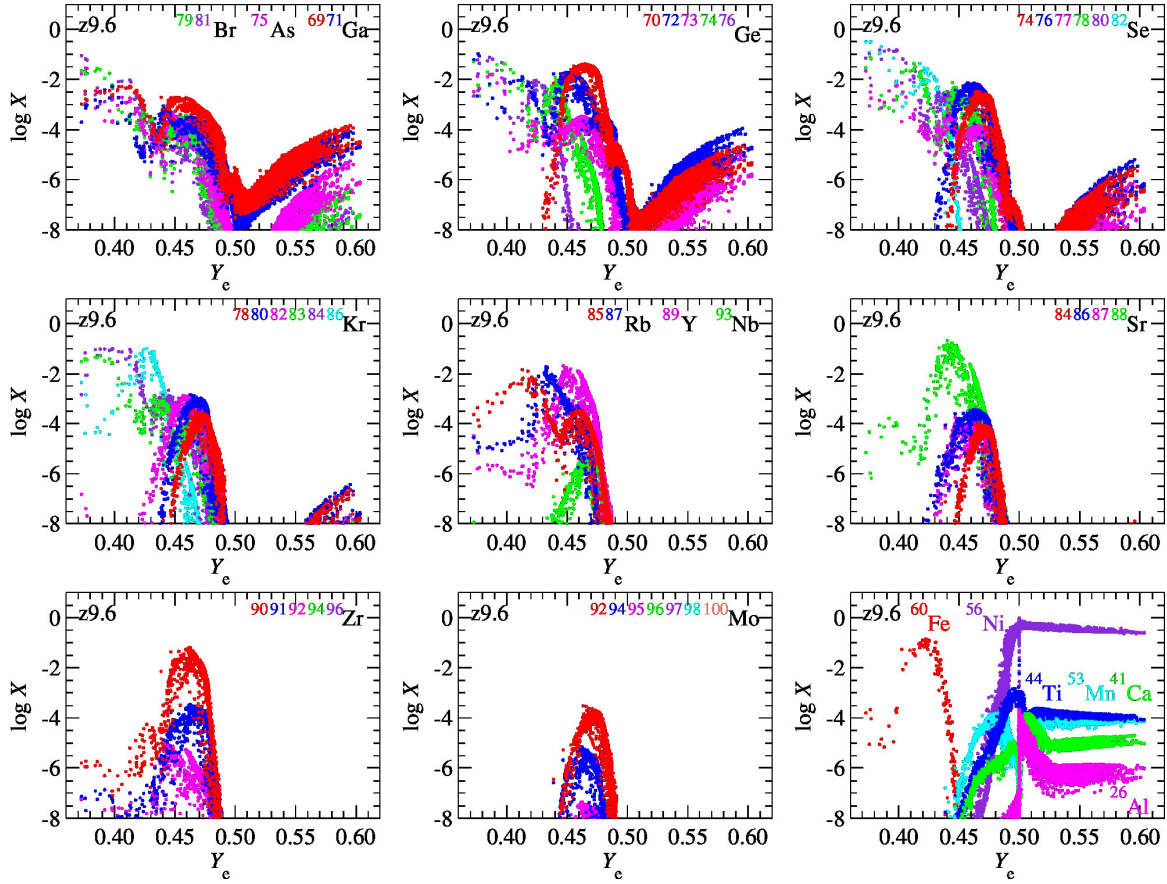


**Figure 9.** Same as Figure 8, but for the stable isotopes of Br, As, and Ga (left-top), Ge (middle-top), Se (right-top), Kr (left-middle), Rb, Y, and Nb (middle), Sr (right-middle), Zr (left-bottom), Mo (middle-bottom), and the radioactive isotopes  $^{26}\text{Al}$ ,  $^{41}\text{Ca}$ ,  $^{44}\text{Ti}$ ,  $^{53}\text{Mn}$ ,  $^{60}\text{Fe}$ , and  $^{56}\text{Ni}$  (right-bottom).

**Table 3.** Top 5 Production Factors

Model	1	2	3	4	5
e8.8	$^{86}\text{Kr}$ 354	$^{87}\text{Rb}$ 260	$^{82}\text{Se}$ 252	$^{74}\text{Se}$ 222	$^{88}\text{Sr}$ 210
z9.6	$^{82}\text{Se}$ 168	$^{88}\text{Sr}$ 166	$^{90}\text{Zr}$ 123	$^{74}\text{Se}$ 110	$^{87}\text{Rb}$ 102
u8.1	$^{74}\text{Se}$ 149	$^{90}\text{Zr}$ 82.6	$^{70}\text{Ge}$ 47.9	$^{78}\text{Kr}$ 38.9	$^{64}\text{Zn}$ 33.8
s11	$^{64}\text{Zn}$ 1.48	$^{45}\text{Sc}$ 1.01	$^{60}\text{Ni}$ 0.857	$^{32}\text{S}$ 0.743	$^{40}\text{Ca}$ 0.632
s15	$^{74}\text{Se}$ 24.8	$^{90}\text{Zr}$ 15.4	$^{78}\text{Kr}$ 6.97	$^{64}\text{Zn}$ 6.10	$^{70}\text{Ge}$ 5.36
s27	$^{74}\text{Se}$ 43.1	$^{78}\text{Kr}$ 35.4	$^{92}\text{Mo}$ 30.7	$^{90}\text{Zr}$ 17.2	$^{84}\text{Sr}$ 12.5

tion of the ejecta that originates in neutron-rich matter ( $Y_e < 0.4975$ ,  $M_{\text{ej},n}$  in Table 2) for a given species. For low-mass models e8.8, z9.6, and u8.1, the light trans-iron isotopes of  $A = 64\text{--}90$  are almost exclusively produced in neutron-rich ejecta, whereas proton-rich matter plays a minor role (see also Figs. 8 and 9). The subdominant roles of SNe from massive progenitors (represented by s11, s15, and s27) to production of these species can be understood as a result of the small mass of neutron-rich ejecta for these stars ( $M_{\text{ej},n}$  in Table 2 and Fig. 2).

Among massive models, s27 has a relatively larger amount of neutron-rich ejecta compared to the two others, with  $Y_e$  down to  $\sim 0.4$ . This is a consequence of the fact that model s27 exhibits an earlier explosion with a rapidly increasing shock radius because of prominent SASI activity that is absent in other models. These neutron-rich ejecta lead to a relatively flat trend of production factors in this model, similar to what we found for e8.8 and z9.6 (Figs. 10 and 11). The bottom-panel of Figure 11 indicates, however, that about a half of

species between  $A = 64$  and  $90$  originate from neutron-rich and proton-rich ejecta. In fact, 43% of  $^{64}\text{Zn}$  in s27 comes from the proton-rich ejecta. As described in 3.1.3, a weak  $\nu p$ -process is responsible for the production of these isotopes in the proton-rich ejecta. Greater entropies of the ejecta (Fig. 3), slower expansion compared to those for low-mass models, and higher neutrino luminosities and mean energies also enhance the efficiency of the  $\nu p$ -process.

#### 4.4. $^{48}\text{Ca}$

Models e8.8 and z9.6 exhibit appreciable production factors of  $^{48}\text{Ca}$  (18.9 and 18.6, respectively), which is made in neutron-rich NSE (or  $\alpha$ -deficient QSE, Meyer et al. 1996; Wanajo et al. 2013a) as can be seen in Figures 6 and 8 (middle-top panels,  $Y_e \sim 0.4$ ). The amounts are still not large enough to regard these low-mass SNe as the main contributors of  $^{48}\text{Ca}$ , although a reduction of the entropies by about 30% would lift the values to a satisfactory level (Wanajo et al. 2013a). A rare class of high-density SNe Ia, in which similar physical conditions are expected, has also been suggested as a possible source of  $^{48}\text{Ca}$  (Woosley 1997).

#### 4.5. Zn isotopes

One of the outstanding features of our nucleosynthesis result is production of all the stable isotopes of Zn ( $A = 64, 66, 67, 68$ , and  $70$ ), an element whose origin remains a mystery. Among our explored models, the low-mass models e8.8 and z9.6 exhibit nearly flat production factors over  $A = 64$ – $70$ . This fact implies that the element Zn, or all their stable isotopes, could originate from ECSNe or low-mass CCSNe as represented by e8.8 and z9.6, respectively. As can be seen in the right-bottom panel of Figure 8, Zn isotopes are predominantly made in neutron-rich ejecta with  $Y_e \sim 0.4$ – $0.5$ ; and models e8.8 and z9.6 produce a sufficient amount of ejecta in this range to contribute most of the Galactic inventory of Zn. There is still a discrepancy of a factor of ten between the largest ( $^{66}\text{Zn}$ ) and smallest ( $^{67}\text{Zn}$ ) production factors, which might be cured if the  $Y_e$  distributions for these models were slightly modified. CCSNe represented by u8.1 cannot be the single source of all Zn isotopes because of the descending trend of production factors (Fig. 13). Model s27, which shows a flat trend of production factors, cannot be representative of Zn contributors either because of the small production factors (1.2–5.2).

To date, only hypernova models (Umeda & Nomoto 2002; Tominaga 2007; Nomoto et al. 2013) have been proposed as sources of Zn (except for an ECSN model in Wanajo et al. 2011a). In their hypernova models high

entropies of ejecta lead to strong  $\alpha$ -rich freeze-out from nuclear equilibrium, resulting in an appreciable production of  $^{64}\text{Zn}$ . This mechanism, however, does not co-produce the other isotopes, which makes this scenario less appealing as an explanation for the origin of the element Zn. As described in § 3.1.3, the  $\nu p$ -process also produces  $^{64}\text{Zn}$  only, and therefore cannot be the main mechanism responsible for making Zn.

#### 4.6. Light trans-iron elements

The nearly flat production factors over wide range of  $A = 64$ – $90$  (except for Ga and As; Fig. 11) in e8.8 and z9.6 also suggest that such low-mass SNe are the dominant sources of light trans-iron elements from Zn to Zr as suggested by Wanajo et al. (2011a) if their mass window is  $\Delta M_{\text{prog}} \sim 0.5$ – $1$ . This is a consequence of the fact that the abundant neutron-rich ejecta for these models (Fig. 2) cover the range of  $Y_e$  (down to  $\sim 0.40$ ) where the productions of these species become maximal (Figs. 8 and 9). By contrast, the results for model u8.1 (with a similar pre-SN core structure to that of z9.6) imply that such SNe can only be a source of the proton-rich isotopes of these trans-iron elements. This is due to the small amount of neutron-rich ejecta with  $Y_e \sim 0.40$ – $0.45$ .

In previous studies, the production of such light trans-iron species has often been attributed to the weak  $s$ -process (e.g. Käppeler et al. 2011). Woosley & Heger (2007) showed that the  $s$ -process in massive stars produces appreciable amounts of light trans-iron isotopes but only between  $A = 65$ – $85$  with a descending trend of production factors. Moreover, Sukhbold et al. (2016) pointed out that such light trans-iron species were sizably underproduced in their work because a large number of stars formed black holes instead of exploding and therefore did not contribute weak  $s$ -process nuclides. We speculate that the weak  $s$ -process in massive stars might still be responsible for Ga and As, which are underproduced in our models e8.8 and z9.6 (Figs. 10 and 11).

#### 4.7. $^{92}\text{Mo}$

It is interesting to note that model s27 gives abundant  $^{92}\text{Mo}$  (with the third largest production factor, 30.7, in Table 3), an important  $p$ -nuclide whose astrophysical origin has been a long-lasting problem. In our case  $^{92}\text{Mo}$  is made in slightly neutron-rich ejecta ( $Y_e \sim 0.47$ , see middle panel of Fig. 6 and middle-bottom panel of Fig. 9) during nuclear equilibrium (as suggested by Hoffman et al. 1996; Wanajo 2006). With a production factor of  $\sim 30$ , such a type of CCSNe, i.e., relatively early explosions with dense outer envelopes, s27-like explosions would need to account for  $\sim 30\%$  of all CC-

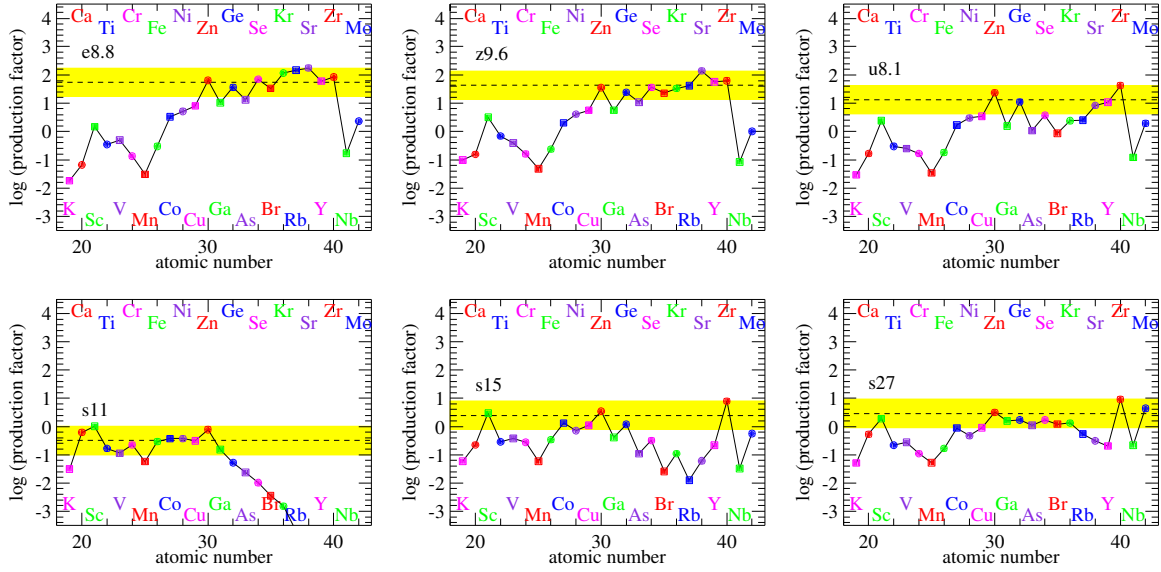


**Figure 10.** Elemental mass fractions in the total ejecta relative to their solar values (Lodders 2003), or production factors, for all SN models. In each panel, the normalization band, which is defined as the range between the maximum value and one-tenth of that, is indicated in yellow with the median value (dashed line).

**Table 4.** Masses of Radioactive Isotopes in the Innermost Ejecta ( $M_{\odot}$ )

Model	$^{26}\text{Al}$	$^{41}\text{Ca}$	$^{44}\text{Ti}$	$^{53}\text{Mn}$	$^{60}\text{Fe}$	$^{56}\text{Ni}$	$^{57}\text{Ni}$
e8.8	4.39E-08	1.96E-07	2.06E-06	1.11E-06	3.61E-05	2.93E-03	1.01E-04
z9.6	1.29E-07	1.16E-07	2.41E-06	1.61E-06	3.14E-05	2.51E-03	9.15E-05
u8.1	4.77E-08	5.77E-08	1.97E-06	1.45E-06	6.65E-07	1.60E-03	7.33E-05
s11 <sup>a</sup>	1.22E-09	1.50E-07	1.19E-06	2.53E-06	1.96E-20	3.86E-03	8.75E-05
s15 <sup>a</sup>	1.07E-08	2.25E-07	1.71E-06	4.46E-06	2.44E-18	6.05E-03	1.16E-04
s27 <sup>a</sup>	2.53E-08	4.56E-07	3.31E-06	5.89E-06	1.14E-06	5.57E-03	1.49E-04

<sup>a</sup> Values for these models should be taken as lower limits (see text).

SNe to explain the solar abundance of  $^{92}\text{Mo}$ . A potential problem is that the other  $p$ -isotope  $^{94}\text{Mo}$  cannot be made in neutron-rich nuclear equilibrium (Hoffman et al. 1996; Wanajo 2006). The  $\nu p$ -process in the neutrino-driven wind may, however, add these isotopes with a high  $^{94}\text{Mo}/^{92}\text{Mo}$  ratio (Pruet et al. 2006; Wanajo 2006; Wanajo et al. 2011b). Note that we do not find large production factors for the  $p$ -isotopes of Ru and Pd as in Pruet et al. (2006). This is due to the fact that these isotopes were made by the  $\nu p$ -process (§ 3.1.3) in their late-time ( $\gtrsim 1$  s) wind ejecta with high entropies ( $S \sim 70 k_{\text{B}}$ ), while the hydrodynamical simulations of models s15 and s27 stopped at  $\sim 0.8$  s after core bounce with entropies still below  $S = 50 k_{\text{B}}$ .

#### 4.8. $^{56}\text{Ni}$

The masses of  $^{56}\text{Ni}$  ejected from all models are listed in Table 4 (7th column), along with those of  $^{57}\text{Ni}$  (last

column). These values, ranging from  $\sim 0.002$ – $0.006 M_{\odot}$ , are about one order of magnitude smaller than typical observed values (e.g.,  $0.07 M_{\odot}$  for SN 1987A Bouchet et al. 1991). The  $^{56}\text{Ni}$  masses in our study should be taken, however, as lower limits for the massive models s11, s15, and s27, for which we omitted the outer envelopes including large parts of the Si/O layer. We therefore likely underestimate the amount of  $^{56}\text{Ni}$  produced by explosive nucleosynthesis in the supernova shock. Moreover, 2D models face a generic difficulty in determining the amount of  $^{56}\text{Ni}$  made by explosive burning in the shock, since the shocked material is funneled around the neutrino-driven outflows onto the proto-neutron star with little mixing by the Kelvin-Helmholtz instability into the neutrino-driven ejecta (Müller 2015). The production of  $^{56}\text{Ni}$  by explosive burning also depends on the post-shock temperatures, and could be related

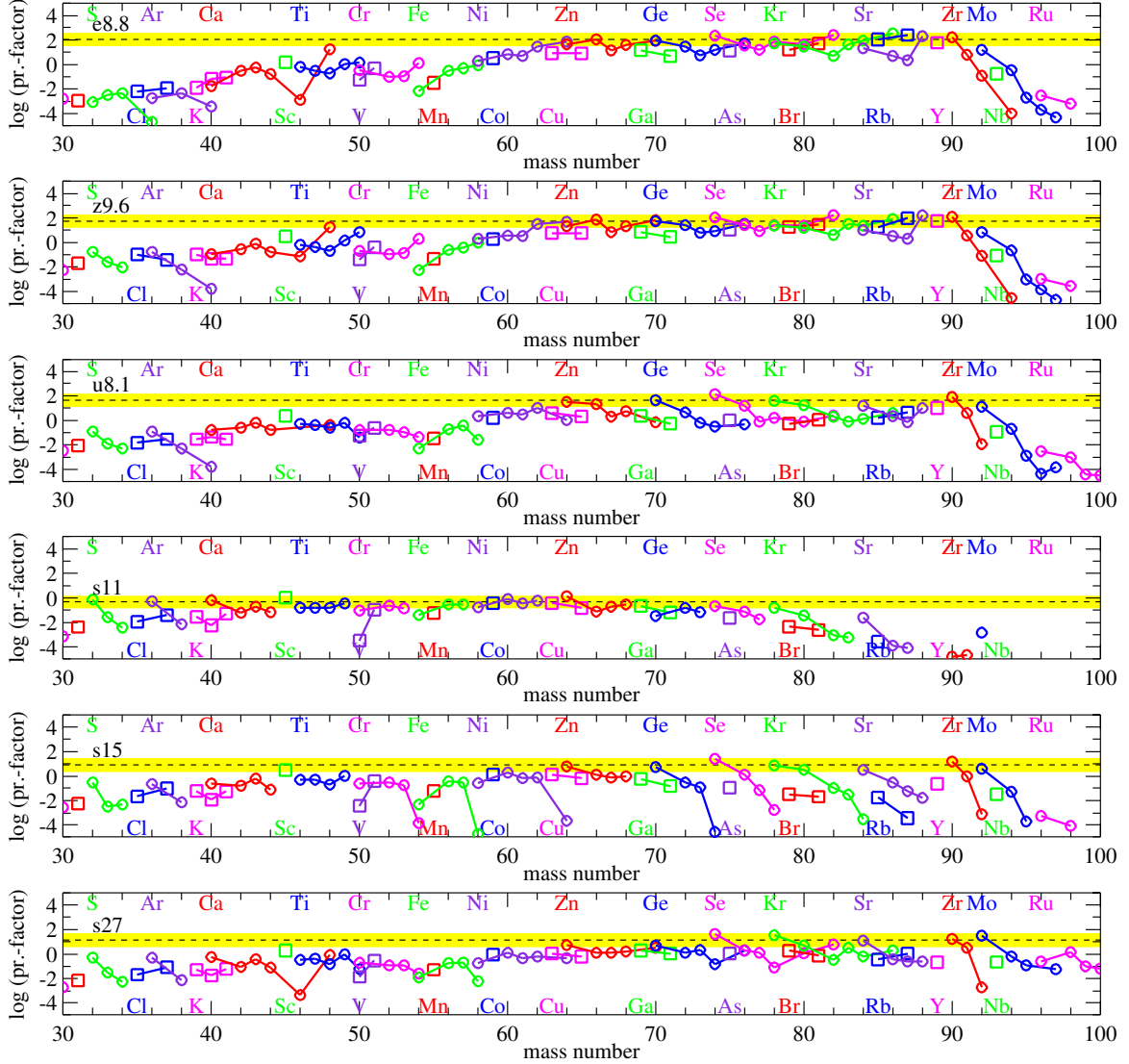


**Figure 11.** Same as Figure 10, but for isotopic mass fractions.

to the slow rise of the explosion energy to only  $(0.3\text{--}1.5) \times 10^{50}$  erg at the end of the simulations.

In addition, the core-collapse simulations of s15 and s27 stopped at a time when accretion was still ongoing and the mass ejection rate in the neutrino-driven outflows was still high, so that we may miss some late-time contribution to  $^{56}\text{Ni}$  in the neutrino-driven ejecta (see, e.g., Wongwathanarat et al. 2016). In fact, the late-time ejecta of s15 and s27 are mostly proton-rich and are dominated by  $^{56}\text{Ni}$  and  $\alpha$ -particles (Fig. 4 and the right-bottom panel of Fig. 9).

For the low-mass models e8.8, z9.6, and u8.1, the listed values can be regarded as the final ones; the  $^{56}\text{Ni}$  mass is definitely very small ( $\sim 0.002\text{--}0.003 M_{\odot}$ ) for these cases. It has already been argued before for e8.8 (Kitauro et al. 2006; Wanajo et al. 2011a; Wanajo 2013), that the small  $^{56}\text{Ni}$  may be consistent with the

value estimated for some observed low-luminosity supernovae (e.g., Hendry et al. 2005; Pastorello et al. 2007) with small ejecta masses. The  $^{56}\text{Ni}$  mass and the other explosion properties of the three low-mass models are also consistent with the remnant composition and reconstructed light curve of the Crab supernova SN 1054 (Smith 2013; Tominaga 2013; Moriya et al. 2014). From the nucleosynthetic point of view, low-mass iron core supernovae thus appear an equally viable explanation for these events compared to ECSNe.

#### 4.9. $^{60}\text{Fe}$ and other radioactive isotopes

The low-mass models e8.8 and z9.6 produce appreciable amounts of  $^{60}\text{Fe}$ ,  $3.61 \times 10^{-5} M_{\odot}$  and  $3.14 \times 10^{-5} M_{\odot}$ , respectively (6th column in Table 4), which is comparable to the IMF-averaged ejection mass from CC-SNe,  $(2.70\text{--}3.20) \times 10^{-5} M_{\odot}$  in Sukhbold et al. (2016).

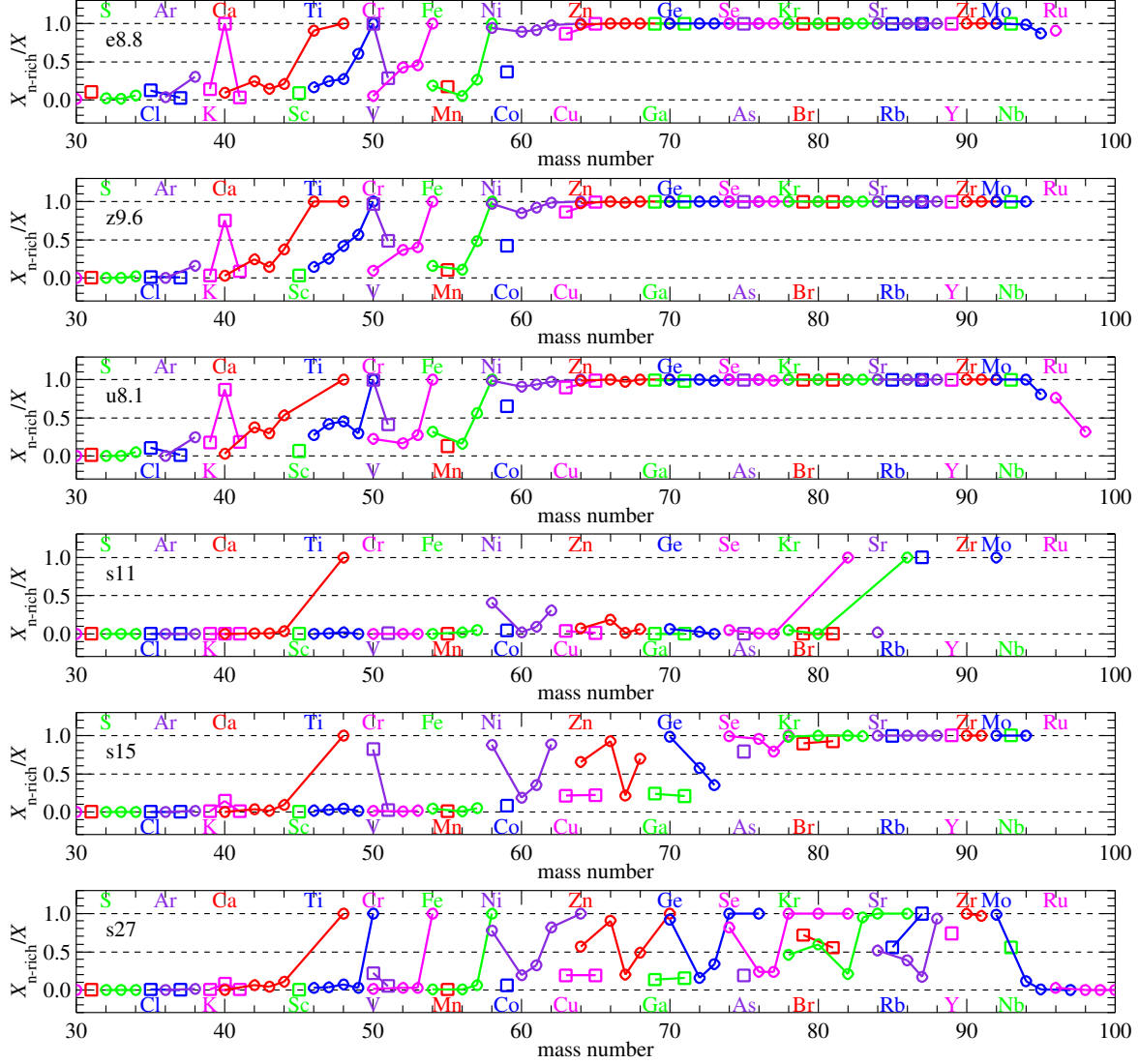


**Figure 12.** Fraction of isotopic yields contributed by neutron-rich matter ( $Y_e < 0.4975$ ,  $M_{\text{ej},n}$  in Table 2).  $X_{n\text{-rich}}/X = 1.0$  and 0.0 mean that a given isotope originates exclusively from neutron-rich and proton-rich ejecta, respectively.

Note that, in massive stars,  $^{60}\text{Fe}$  is produced by successive neutron captures from iron isotopes (Timmes et al. 1995) in the outer envelope, which is not included in our analysis of the massive models s11, s15, and s27. In e8.8 and z9.6  $^{60}\text{Fe}$  forms in neutron-rich NSE ( $Y_e \sim 0.42\text{--}0.43$ , right-bottom panel of Fig. 9) as suggested by Wanajo et al. (2013b). This indicates that ECSNe or low-mass CCSNe account for at least  $\sim 10\%$  (see  $f_{\text{e8.8}}$  and  $f_{\text{z9.6}}$  in § 4.2) of live  $^{60}\text{Fe}$  in the Galaxy. Models other than e8.8 and z9.6 produce little  $^{60}\text{Fe}$  in their innermost ejecta because of their small masses of neutron-rich ejecta.

Table 4 also lists the masses of other important radioactive isotopes  $^{26}\text{Al}$ ,  $^{41}\text{Ca}$ ,  $^{44}\text{Ti}$ , and  $^{53}\text{Mn}$ , which are, however, negligibly small compared to the contribution from the outer envelopes of massive stars (and

from neutrino-driven wind for  $^{44}\text{Ti}$ , Wongwathanarat et al. 2016). Recent work by Sukhbold et al. (2016) suggested the IMF-averaged amount of  $^{26}\text{Al}$  from massive stars to be  $(2.80\text{--}3.63) \times 10^{-5} M_{\odot}$ . Their resultant mass ratio of  $^{60}\text{Fe}$  to  $^{26}\text{Al}$ ,  $\sim 1$  (although a factor of 2 smaller than previous estimates, e.g., Woosley & Heger 2007), conflicts with the ratio inferred from gamma-ray observation,  $\sim 0.34$  (Wang et al. 2007). Taking the observational value as a constraint, this would suggest that Sukhbold et al. (2016) overestimated the  $^{60}\text{Fe}$  mass about a factor of 3. The reason for this can be attributed to uncertainties in the relevant reaction rates (Woosley & Heger 2007; Tur et al. 2010), while for our cases  $^{60}\text{Fe}$  forms in nuclear equilibrium and thus individual reactions are irrelevant. If this is the case, ECSNe or low-



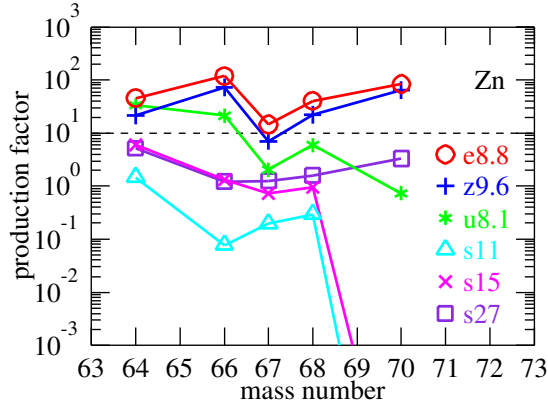


**Figure 13.** Production factors of Zn isotopes (nucleosynthetic yields relative to solar values) for all models indicated by different symbols in the legend.

mass SNe can contribute to live  $^{60}\text{Fe}$  up to  $\sim 30\%$  of the amount in the Galaxy.

## 5. CONCLUSIONS

We have examined the nucleosynthesis in the innermost ejecta ( $0.01\text{--}0.03 M_{\odot}$ ) of CCSNe, including ECSNe, by adopting thermodynamic trajectories obtained from self-consistent (general-relativistic with one exception) 2D core-collapse supernova explosion models with multi-group neutrino transport. We explored the six models e8.8 ( $8.8 M_{\odot}$  ECSN,  $1 Z_{\odot}$ ), z9.6 ( $9.6 M_{\odot}$ ,  $0 Z_{\odot}$ ), u8.1 ( $8.1 M_{\odot}$ ,  $10^{-4} Z_{\odot}$ ), s11 ( $11.2 M_{\odot}$ ,  $1 Z_{\odot}$ ), s15 ( $15.0 M_{\odot}$ ,  $1 Z_{\odot}$ ), and s27 ( $27.0 M_{\odot}$ ,  $1 Z_{\odot}$ ), with a progressively shallower core-density gradient in that order (Fig. 8 in Janka et al. 2012). In this paper, we focused on the effects of these differences in the pre-SN core-density structure on the nucleosynthesis, and did not attempt to address the exact dependence of the nucleosynthesis on mass or metallicity (owing to the limited number of available models). Our results indicate, however, that “low-mass” progenitors close to the iron core formation limit (which are characterized by off-center ignition of oxygen burning) stand apart from “massive stars” due to shared structural and evolutionary features: The low-mass models e8.8, z9.6, and u8.1 (near the low-mass end of SN progenitors) have abundant neutron-rich matter (40–50%) in their ejecta because of fast shock expansion after the onset of the explosion. By contrast, proton-rich matter dominates the ejecta of the more massive models s11, s15, and s27 by far, because slower shock expansion allows neutrino interactions to efficiently raise  $Y_e$ .

For this reason, our nucleosynthesis calculations in post-processing steps resulted in remarkably different outcomes between the low-mass (e8.8, z9.6, and u8.1) and massive (s11, s15, and s27) models. We determined that low-mass SNe, in particular those represented by

e8.8 (ECSN) and z9.6, could be the dominant source of light trans-iron elements from Zn to Zr (except for Ga and As), if these events account for  $\sim 8\text{--}14\%$  (or a mass window of  $\Delta M_{\text{prog}} = 0.5\text{--}1 M_{\odot}$ ) of all CCSNe (including ECSNe). These species are made predominantly in neutron-rich ejecta during nuclear-equilibrium phases. Good agreement of the nucleosynthetic yields with the solar-abundance pattern over a wide range of isotopes with  $A = 64\text{--}90$  strongly supports our conclusion, which sets this candidate site apart from other previously suggested astrophysical sites, e.g., hypernovae (as origin of Zn, Umeda & Nomoto 2002; Tominaga 2007; Nomoto et al. 2013) and the weak  $s$ -process in massive stars (as origin of light trans-iron elements, Woosley & Heger 2007; Käppeler et al. 2011). These SNe (e8.8 and z9.6) could also be important sources of the neutron-rich isotope  $^{48}\text{Ca}$  and the live radioactive species  $^{60}\text{Fe}$  in the Galaxy, and supplement the chemogalactic contribution of other sites such as rare SNe Ia (Woosley 1997) with high ignition densities and massive stars (e.g., Sukhbold et al. 2016). Model u8.1, however, was found to have contributions of proton-rich isotopes of light trans-iron elements only, despite its similar (but slightly shallower) core-density gradient compared to that of z9.6.

We found that the innermost ejecta of massive SNe make little contributions to the chemical inventory of the Galaxy, except for proton-rich isotopes of light trans-iron elements (in s15 and s27). The most massive model s27 exhibited an interesting production of  $p$ -nucleus  $^{92}\text{Mo}$ , which could explain the solar amount of  $^{92}\text{Mo}$  if such s27-like events accounted for  $\sim 30\%$  of all CCSNe. This was traced back to a sizable amount of slightly neutron-rich ejecta ( $Y_e \sim 0.47$ ) with moderately high entropies ( $\sim 30 k_B/\text{nuc}$ ), in which  $^{92}\text{Mo}$  is made in nuclear equilibrium (Hoffman et al. 1996; Wanajo 2006). Note that our calculations did not include the outer envelopes, from which iron-group and lighter elements would be ejected in these massive SNe. Instead, we focused mostly on the neutrino-processed ejecta during the first few hundreds of milliseconds after shock revival. This implies that our results on the production of iron-group and trans-iron elements in the more massive models (s11, s15, s27) are only indicative of the overall nucleosynthesis and may miss important contributions. For the ECSN progenitor e8.8 and the ECSN-like models z9.6 and u8.1, the nucleosynthesis in this range is essentially complete, barring minor contributions from the neutrino-driven wind that follows after our simulations were terminated.

Aside from the fact that the nucleosynthesis in s11, s15, and s27 is not yet complete, some further caveats should be added to our conclusions here. Although nu-

cleosynthesis calculations based on self-consistent 2D core-collapse supernova models represent a fundamental improvement over previous 1D studies (which mostly excluded neutrino-processed ejecta), the explosion dynamics in 3D has emerged as noticeably different from 2D (see Janka et al. 2016; Müller 2016, for recent reviews). The interaction between buoyant, neutrino-heated ejecta and accretion downflows tends to brake both outflows and downflows (Melson et al. 2015; Müller 2015) and could therefore modify the final  $S$  and  $Y_e$  in the neutrino-driven ejecta. So far, model z9.6 offers the only opportunity for a direct comparison of the nucleosynthesis conditions. For this progenitor, 3D effects only moderately affect the explosion dynamics (Melson et al. 2015) and may only slightly raise the minimum  $Y_e$  in the ejecta without fundamentally changing the neutron-rich nucleosynthesis in this progenitor (Müller 2016). The situation for other low-mass iron core-collapse supernovae and ECSNe is likely similar.

For more massive progenitors, larger systematic effects on the nucleosynthesis conditions in 3D cannot be excluded. The results of Müller (2015) for an  $11.2M_\odot$  model suggest that the outflow velocities (which affect the  $Y_e$ ) and the terminal entropies in 3D can be considerably lower, but these results have yet to be borne out for a broader range of progenitors. The mixing of shocked material into the neutrino-heated ejecta is likely more efficient in 3D, and will affect the contribution of explosive nucleosynthesis in the shock to the total ejecta, because this matter is swept outward instead of being accreted onto the new-born neutron star. Along with the low explosion energies of the massive 2D models, this may explain the unusually small mass of  $^{56}\text{Ni}$  found in our calculations.

Effects that may change the final  $Y_e$  in the neutrino-processed ejecta by altering the neutrino emission also warrant further exploration. Aside from uncertainties in the neutrino microphysics, the impact of the genuinely three-dimensional LESA (lepton-number emission self-sustained asymmetry) instability (Tamborra et al. 2014; Janka et al. 2016) on the nucleosynthesis conditions deserves investigation. As LESA produces a global asymmetry in the flux difference between electron neutrinos and antineutrinos, it will contribute to a spread in the  $Y_e$ -distribution in the ejecta. A detailed analysis of LESA effect in z9.6 is currently underway; the neutron-rich bubbles in the early ejecta remain a robust feature

for this progenitor also in the presence of LESA (Melson et al., in preparation).

In summary, while our conclusions for low-mass SNe might be robust, those for massive models should only be taken as suggestive. Eventually, successful explosion models of such massive SNe in 3D are required for drawing firmer conclusions. It is, however, also important to scan the low-mass end of the progenitor range with a finer resolution in progenitor mass. While Wanajo et al. (2011a, 2013a,b) suggested that ECSNe could be important contributors of light trans-iron elements (including Zn),  $^{48}\text{Ca}$ , and  $^{60}\text{Fe}$ , our results show that CC-SNe near the low-mass end with iron-cores (z9.6) have almost the same nucleosynthetic outcomes. A model (u8.1) with only a slightly shallower core-density gradient resulted in, however, a substantially different result. Stellar evolution models and core-collapse supernova simulations therefore need to better address over which mass range the progenitors possess core-density profiles that are sufficiently steep to produce ECSN-like nucleosynthesis near the low-mass end of the progenitor-mass spectrum.

It should also be noted that we neglect late-time ejecta in the neutrino-driven wind in the present study. These could also contribute to the enrichment of trans-iron species to the Galaxy by a weak  $r$ -process (e.g., Wanajo 2013) and a  $\nu p$ -process (Fröhlich et al. 2006; Pruet et al. 2006; Wanajo 2006). Finally, our result should be tested by a study of Galactic chemical evolution to reproduce the observational signatures of light trans-iron elements in the Galaxy.

This work was supported by the RIKEN iTHES Project, the JSPS Grants-in-Aid for Scientific Research (26400232, 26400237), by the Deutsche Forschungsgemeinschaft through the Excellence Cluster Universe EXC 153 (TJ), and by the European Research Council through grant ERC-AdG No. 341157-COCO2CASA (TJ). We also acknowledge partial support by the Australian Research Council through a Discovery Early Career Researcher Award DE150101145 (BM) and an ARC Future Fellowship FT120100363 (AH). This research was undertaken with the assistance of resources from the Max Planck Computing and Data Facility (using the *hydra* cluster), the Minnesota Supercomputing Institute, the National Computational Infrastructure (NCI), which is supported by the Australian Government, and the Pawsey Supercomputing Centre with funding from the Australian Government and the Government of Western Australia.

## REFERENCES

- Arcones, A., Janka, H.-Th., & Scheck, L. 2007, *A&A*, 467, 1227
- Arcones, A., Fröhlich, C., and Martínez-Pinedo, G. 2012, *ApJ*, 750, 18
- Bouchet, P., Phillips, M. M., Suntzeff, N. B., et al. 1991, *A&A*, 245, 490
- Bruenn, S. W., et al. 2016, *ApJ*, 818, 123
- Buras, R., Rampp, M., Janka, H.-Th., & Kifonidis, K. 2006, *A&A*, 447, 1049
- Audi, G., Wang, M., Wapstra, A. H., Kondev, F. G., MacCormick, M., Xu, X., & Pfeiffer, B. 2012, *Chin. Phys. C*, 36, 1287
- Blondin, J. M., Mezzacappa, A., & DeMarino, C. 2003, *ApJ*, 584, 971
- Cordero-Carrión, I., Cerdá-Durán, P., Dimmelmeier, H., Jaramillo, J. L., Novak, J., & Gourgoulhon, E., *PhRvD*, 79, 024017
- Cybert, R. H., et al. 2010, *ApJS*, 189, 240
- Doherty C. L., Gil-Pons P., Siess L., Lattanzio J. C., Lau H. H. B., 2015, *MNRAS*, 446, 2599
- Fransson, C., & Kozma, C. 2002, *NewAR*, 46, 487
- Fröhlich, C., et al. 2006, *PhRvL*, 96, 142502
- Fujimoto, S., Kotake, K., Hashimoto, M., Ono, M., & Ohnishi, N. 2011, *ApJ*, 738, 61
- Hartmann, D., Woosley, S. E., & El Eid, M. F. 1985, *ApJ*, 297, 837
- Heger, A. & Woosley, S. E. 2010, *ApJ*, 724, 341
- Hendry, M. A., et al. 2005, *MNRAS*, 359, 906
- Hoffman, R. D., Woosley, S. E., Fuller, G. M., & Meyer, B. S. 1996, *ApJ*, 460, 478
- Hoffman, R. D., Pruet, J., Fisker, J. L., Janka, H.-T., Buras, R., & Woosley, S. E. 2007, *arXiv:0712.2847*
- Hoffman, R. D., Müller, B., & Janka, H.-T. 2008,
- Ibeling, D., & Heger, A. 2013, *ApJL*, 765, 43
- Janka, H.-Th., Müller, B., Kitaura, F. S., & Buras, R. 2008, *A&A*, 485, 199
- Janka, H.-T., Hanke, F., Hudepohl, L., et al. 2012, *PTEP*, 2012, 01A309
- Janka, H.-T., Melson, T., & Summa, A. 2016, *Ann. Rev. Nucl. Part. Sci.*, 66, 341
- Jones, S., Hirschi, R., Nomoto, K., Fischer, T., Timmes, F. X., Herwig, F., Paxton, B., Toki, H., Suzuki, T., Martínez-Pinedo, G., Lam, Y. H., Bertolli, M. G., *ApJ*, 772, 150
- Jones, S., Hirschi, R., Nomoto, K., *ApJ*, 797, 83
- Jones, S., Roepke, F. K., Pakmor, R., Seitenzahl, I. R., Ohlmann, S.T., Edelmann, P. V. F., *arXiv:1602.05771*
- Käppeler, F., Gallino, R., Bisterzo, S., & Aoki, W. 2011, *RvMP*, 83, 157
- Kasen, D., Woosley, S. E. 2009, *ApJ*, 703, 2005
- Kitaura, F. S., Janka, H.-Th., & Hillebrandt, W. 2006, *A&A*, 450, 345
- Kuroda, T., Wanajo, S., & Nomoto, K. 2008, *ApJ*, 672, 1068
- Langanke, K. & Martínez-Pinedo, G. 2001, *At. Data Nucl. Data Tables*, 79, 1
- Limongi, M., & Chieffi, A. 2006, *ApJ*, 647, 483
- Lodders, K. 2003, *ApJ*, 591, 1220
- McLaughlin, G. C., Fuller, G. M., & Wilson, J. R. 1996, *ApJ*, 472, 440
- Melson, T., Janka, H.-T., & Marek, A. 2015, *ApJL*, 801, L24
- Meyer, B. S., Krishnan, T. D., & Clayton, D. D. 1996, *ApJ*, 462, 825
- Meyer, B. S., McLaughlin, G. C., & Fuller G. M. 1998, *PhRvC*, 58, 3696
- Meyer, B. S., Krishnan, T. D., & Clayton, D. D. 1998, *ApJ*, 498, 808
- Moriya, T. J., Tominaga, N., Langer, N., Nomoto, K., Blinnikov, S. I., Sorokina, E. I., 2014, *A&A*, 569, A57
- Müller, B., Janka, H.-Th., & Dimmelmeier, H. 2010, *ApJS*, 189, 104
- Müller, B., Janka, H.-T., & Marek, A. 2012a, *ApJ*, 756, 84
- Müller, B., Janka, H.-Th., & Heger, A. 2012b, *ApJ*, 761, 72
- Müller, B. 2015, *MNRAS*, 453, 287
- Müller, B. 2016, *PASA*, 33, e048
- Ning, H., Qian, Y. -Z., & Meyer, B. S. 2007, *ApJL*, 667, L159
- Nomoto, K. 1987, *ApJ*, 322, 206
- Nomoto, K., Kobayashi, C., & Tominaga, N. 2013, *ARA&A*, 51, 457
- Panov, I. V. & Janka, H.-Th. 2009, *A&A*, 494, 829
- Pastorello, A., et al. 2007, *Nature*, 449, 1
- Perego, A., Hempel, M., Fröhlich, C., et al. 2015, *ApJ*, 806, 275
- Pllumbi, E., Tamborra, I., Wanajo, S., Janka, H.-T., Hudepohl, L. 2015, *ApJ*, 808, 108
- Poelarends, A. J. T., Herwig, F., Langer, N., & Heger, A. 2008, *ApJ*, 675, 614
- Pruet, J., Woosley, S. E., Buras, R., & Janka, H.-Th. 2005, *ApJ*, 623, 325
- Pruet, J., Hoffman, R. D., Woosley, S. E., Buras, R., & Janka, H.-Th. 2006, *ApJ*, 644, 1028
- Rampp, M. & Janka, H.-Th., 2002, *A&A*, 396, 361
- Rauscher, T., Heger, A., Hoffman, R. D., & Woosley, S. E. 2002, *ApJ*, 576, 323
- Smith, N. 2013, *MNRAS*, 434, 102

- Sukhbold, T., Ertl, T., Woosley, S. E., Brown, J. M., & Janka, H.-T. 2016, *ApJ*, 821, 38
- Tamborra, I., Hanke, F., Janka, H.-T., Müller, B., Raffelt, G. G., Marek, A. 2014, *ApJ*, 792, 96
- Timmes, F. X., Woosley, S. E., Hartmann, D. H., et al. 1995, *ApJ*, 449, 204
- Thielemann, F.-K., Nomoto, K., & Hashimoto, M.-A. 1996, *ApJ*, 460, 408
- Tominaga, N., Umeda, H., & Nomoto, K. 2007, *ApJ*, 660, 516
- Tominaga, N., Blinnikov, S. I., Nomoto, K., 2013, *ApJL*, 771, L12
- Tur, C., Heger, A., & Austin, S. M. 2010, *ApJ*, 718, 357
- Umeda, H. & Nomoto, K. 2002, *ApJ*, 565, 385
- Wanajo, S., Kajino, T., Mathews, G. J., & Otsuki, K. 2001, *ApJ*, 554, 578
- Wanajo, S. 2006, *ApJ*, 647, 1323
- Wanajo, S., Nomoto, K., Janka, H.-T., Kitaura, F. S., Müller, B. 2009, *ApJ*, 695, 208
- Wanajo, S., Janka, H.-T., & Müller, B. 2011, *ApJ*, 726, L15
- Wanajo, S., Janka, H.-T., & Kubono, S. 2011, *ApJ*, 729, 46
- Wanajo, S., Janka, H.-T., & Müller, B. 2013, *ApJL*, 767, L26
- Wanajo, S., Janka, H.-T., & Müller, B. 2013, *ApJL*, 774, L6
- Wanajo, S. 2013, *ApJL*, 770, L22
- Wang, W., Harris, M. J., Diehl, R., et al. 2007, *A&A*, 469, 1005
- Woosley, S. E., Hartmann, D. H., Hoffman, R. D., & Haxton, W. C. 1990, *ApJ*, 356, 272
- Woosley, S. E. & Hoffman, R. D. 1992, *ApJ*, 395, 202
- Woosley, S. E., Wilson, J. R., Mathews, G. J., Hoffman, R. D., & Meyer, B. S. 1994, *ApJ*, 433, 229
- Woosley, S. E., & Weaver, T. A. 1995, *ApJ*, 101, 181
- Woosley, S. E. 1997, *ApJ*, 476, 801
- Woosley, S. E., Heger, A., & Weaver, T. A. 2002, *RvMP*, 74, 1015
- Woosley, S. E., & Heger, A. 2007, *PhR*, 442, 269
- Woosley, S. E., & Heger, A. 2010, *ApJ*, 810, 34